Organic geochemical characteristics, mineralogy, petrophysical properties, and shale gas prospects of the Wufeng–Longmaxi shales in Sanquan Town of the Nanchuan District, Chongqing

Yijun Zheng, Yuhong Liao, Yunpeng Wang, Yongqiang Xiong, and Ping'an Peng

AUTHORS

YIJUN ZHENG ~ *State Key Laboratory of Organic Geochemistry, Guangzhou Institute of Geochemistry, Chinese Academy of Sciences, Kehua Street 511#, Wushan Road, Tianhe District, Guangzhou 510640, China; College of Earth and Planetary Sciences, University of Chinese Academy of Sciences, Yuquan Road, Beijing 100049, China; zyjln123@sina.com*

Yijun Zheng is currently a Ph.D. student at the State Key Laboratory of Organic Geochemistry, Guangzhou Institute of Geochemistry, Chinese Academy of Sciences. His current work is mainly about shale gas.

YUHONG LIAO ~ *State Key Laboratory of Organic Geochemistry, Guangzhou Institute of Geochemistry, Chinese Academy of Sciences, Kehua Street 511#, Wushan Road, Tianhe District, Guangzhou 510640, China; liaoyh@gig.ac.cn*

Yuhong Liao is an organic geochemist and a research fellow of Guangzhou Institute of Geochemistry, Chinese Academy of Sciences. He earned his B.S. and Ph.D. from Peking University and Guangzhou Institute of Geochemistry, Chinese Academy of Sciences, in 2000 and 2006, respectively. He is currently working on petroleum reservoir geochemistry and unconventional oil and gas. He is the corresponding author of this paper.

YUNPENG WANG ~ *State Key Laboratory of Organic Geochemistry, Guangzhou Institute of Geochemistry, Chinese Academy of Sciences, Kehua Street 511#, Wushan Road, Tianhe District, Guangzhou 510640, China; wangyp@gig.ac.cn*

Yunpeng Wang earned his B.S. and Ph.D. from Lanzhou University and Guangzhou Institute of Geochemistry, Chinese Academy of Sciences, in 1990 and 1996, respectively. He is currently working on gas geochemistry and petroleum system modeling related to unconventional and deep gases. He is the member of the International Committee of Gas Geochemistry.

YONGQIANG XIONG ~ *State Key Laboratory of Organic Geochemistry, Guangzhou Institute of Geochemistry, Chinese Academy of Sciences, Kehua Street 511#, Wushan*

ABSTRACT

Thick marine shales occur in the Wufeng Formation and Longmaxi Formation of Sanquan Town of the Nanchuan District, Chongqing Municipality, which is located on the southeast margin of the Sichuan Basin. However, few details of the characteristics of the Wufeng–Longmaxi shales in this area have been reported. In this study, a well approximately 100 m (~328 ft) deep was drilled. A high-quality shale (total organic carbon [TOC] >2.0 wt. %, clay <40%) interval that was approximately 24 m (~79 ft) thick with an average TOC value of 3.0 wt. % mainly occurs in the Ordovician Wufeng Formation (Katian and Hirnantian) and base of the Silurian Longmaxi Formation (Rhuddanian). Shales with higher TOC values commonly have a higher porosity and specific surface area. Tectonic movements may also have been very important factors that influenced the petrophysical properties of the shales. For example, a detachment layer that resulted from complex tectonic movements is extensive in the Wufeng Formation. The cracks and microcracks in the detachment layer can result in good pore connectivity. Consequently, the detachment layer can be an effective migration pathway. The Longmaxi–Wufeng shales of Sanquan Town are also compared with those of the famous Jiaoye 1 well in the Jiaoshiba shale gas field in the eastern Sichuan Basin. Although the shales in Sanquan Town have considerable shale gas generation potential, the shale gas resource

Road, Tianhe District, Guangzhou 510640, China; xiongyq@gig.ac.cn

Yongqiang Xiong received his Ph.D. in geochemistry from Guangzhou Institute of Geochemistry, Chinese Academy of Sciences, in 2001. His general research interest is oil and gas geochemistry. His present research is focused on the quantitative characterization of the source and maturity of highly mature hydrocarbons.

PING'AN PENG ~ State Key Laboratory of Organic Geochemistry, Guangzhou Institute of Geochemistry, Chinese Academy of Sciences, Kehua Street 511#, Wushan Road, Tianhe District, Guangzhou 510640, China; pinganp@gig.ac.cn

Ping'an Peng is an organic geochemist and research fellow of Guangzhou Institute of Geochemistry, Chinese Academy of Sciences. Ping'an earned his B.S. and Ph.D. from Zhejiang University and Institute of Geochemistry, Chinese Academy of Sciences, respectively. He has worked in petroleum geochemistry for 35 years. In 2013, he was elected as academician of the Chinese Academy of Sciences.

DATASHARE 98

Table S1 is available in an electronic version on the AAPG website (www.aapg.org/datashare) as Datashare 98.

potential in Sanquan Town is probably poor because the escape of shale gas may be accelerated by the detachment layer in destroyed anticlines and synclines.

INTRODUCTION

Shales are commonly regarded as source rocks or caprocks in conventional petroleum exploration (Hunt, 1996). Over the past 10 yr, with the tremendous progress that has been made in the exploration and development of shale oil and shale gas in North America (Kuila and Prasad, 2013), it has been realized that shale can also be an effective unconventional reservoir (Chalmers et al., 2012a). Researchers in China found that lower Paleozoic shales, such as those of the Upper Ordovician Wufeng Formation–lower Silurian Longmaxi Formation (the Wufeng–Longmaxi shales), are similar to the major United States shale gas reservoirs in many respects (Curtis, 2002; Li et al., 2007; Chalmers et al., 2012a; Yang et al., 2016). In recent years, Sinopec and PetroChina have achieved substantial breakthroughs in the Wufeng–Longmaxi Formations of Fuling (located in the eastern Sichuan Basin) and Changning–Weiyuan (located in the southern Sichuan Basin) (Wei et al., 2016). These exploration successes confirmed that the Wufeng–Longmaxi Formations in the Sichuan Basin have prospects for shale gas exploration and development. For example, shale gas production of the Jiaoshiba shale gas field in the Fuling District of the Chongqing Municipality was 1.1, 3.2, and 5.0 billion m^3 (38.8, 113.0, and 176.6 BCF) in 2014, 2015, and 2016, respectively. Because the Wufeng–Longmaxi Formations in the Sichuan Basin had experienced multiphase tectonic movements, the great successes in the Wufeng–Longmaxi Formations of the Jiaoshiba shale gas field, which is also known as the Fuling shale gas field, have attracted the interest of many petroleum geologists (Liang et al., 2012, 2017; Tian et al., 2013; Guo and Zhang, 2014; Guo et al., 2014a; Chen et al., 2015; Guo and Zeng, 2015; Zou et al., 2015). Most scholars believe that shale gas is characterized by relatively short-distance migration (Curtis, 2002) and is mainly constrained by the organic matter (OM) abundance and thickness of the shale (Hao et al., 2013; Ji et al., 2015). However, similar to conventional oil and gas reservoirs, the exploration and statistical results show that most of the shale gas fields in South China are linked to some specific structural traps (Guo and Zeng, 2015). For example, anticlines are the most favorable structural trap for shale gas accumulation and enrichment (Guo and Zeng, 2015).

The petrophysical properties of shales, especially the nanopore structure, are very important for understanding the adsorption capacity, diffusion, and flow of gas in shales (Loucks et al., 2009; Kuila and Prasad, 2013; Mastalerz et al., 2013; Wei et al., 2016; Yang et al., 2016). The intricate pore networks of

shales have been linked to many geologic factors, such as the abundance, type, and maturity of OM, and mineralogy (Ross and Bustin, 2009b; Curtis et al., 2012; Kuila and Prasad, 2013; Milliken et al., 2013; Loucks and Reed, 2014; Cao et al., 2015a; Zhao et al., 2017). Pores in shale can be mainly classified as organic pores, interparticle pores, intraparticle pores, and microfractures (Loucks et al., 2012; Loucks and Reed, 2014; Yang et al., 2016). Researchers have used CO_2 and N_2 composited adsorption isotherms and Hg porosimetry to investigate the complex pore structure of nanopores in shales (Ross and Bustin, 2009b; Kuila and Prasad, 2013; Mastalerz et al., 2013; Cao et al., 2015a; Wei et al., 2016). Mercury injection capillary pressure (MICP) techniques are commonly considered to only be suitable for porosity measurements of pores with diameters greater than 3 nm (Bolton et al., 2000; Cao et al., 2015a), whereas low-temperature CO_2 and N_2 gas adsorption are commonly used to measure the specific surface area and pore volume of pores with pore diameters in the range of 0.33–100 nm (Ross and Bustin, 2009b; Kuila and Prasad, 2013; Wei et al., 2016).

In this study, a shallow core well was drilled in Sanquan Town. Based on the shale cores obtained by the shallow drilling, the sequence stratigraphy, geochemical characteristics of OM, mineralogy, and compositions of major elements were investigated. The CO_2 and N_2 composited adsorption isotherms and Hg porosimetry were used to investigate the complex pore structure of nanopores in the shale, and possible factors that may affect the petrophysical properties of the Wufeng–Longmaxi shales were also discussed. Additionally, field emission scanning electron microscopy (FE-SEM) imaging can provide qualitative information on the pore types (Loucks et al., 2009; Loucks and Reed, 2014; Zhao et al., 2017). Therefore, the pore structures of the Wufeng–Longmaxi shales were also analyzed by FE-SEM.

GEOLOGICAL SETTING

In the Late Ordovician, significant subsidence occurred in the Sichuan Basin (Chen et al., 2014). As a result, a semirestricted stagnant basin (Figure 1A) was formed in southern Sichuan, northeastern Sichuan, eastern Chongqing, and western Hubei (Chen et al., 2015; Liu et al., 2016). The sedimentary environment of the Sichuan Basin was low energy and anoxic during the Late Ordovician–early Silurian (Guo and Zhang, 2014). Two global transgressions occurred (Guo et al., 2014b). As a result, a succession of black, carbonaceous, graptolitic shale and radiolarian graptolitic shale (Luo et al., 2016; Ma et al., 2016) was deposited as the Upper Ordovician Wufeng Formation (O_3), and a succession of black carbonaceous shale and dark gray argillaceous siltstone was deposited as the lower Silurian Longmaxi Formation. Some scholars refer to them together as the Longmaxi shale, in which the fossils include benthic algae, siliceous radiolarians, and abundant graptolites (Guo and Liu, 2013; Guo and Zhang, 2014). In the Sichuan Basin and neighboring regions, the major shale intervals were developed in the Wufeng Formation and the lower part of the Longmaxi Formation, especially near the sedimentary center. Two deposition centers exist where thick black shales of the Wufeng–Longmaxi Formations were deposited. One deposition center occurs in the eastern Sichuan Basin and the other in the southern Sichuan Basin. The black shales gradually thin from the deposition center to provenance area (Figure 1A). In the depth profile, the lower part of the Longmaxi shale consists of black, pyrite-rich graptolitic shale (Luo et al., 2016; Ma et al., 2016), whereas the middle and upper parts are composed of gray–green shale and silty shale because the paleoenvironments gradually transitioned from deep-water shelf facies to shallow-water shelf facies (Liang et al., 2012; Wang et al., 2015b).

In the middle Silurian, the sedimentation rate increased, water became shallower, sediments became coarser, and marine facies evolved into marine–continental alternative facies in the upper Yangtze region (Guo, 2014). Before the Permian, the upper Yangtze region was denuded to some degree. Because of the shallow burial depth (<2000 m [<6562 ft]) that resulted from the uplift and low heat flow (<50 mW·m^{-2}), the Wufeng–Longmaxi shales were immature at this stage (Cao et al., 2015b). In the Permian, the sedimentary environment of the upper Yangtze region was characterized by shallow water and a carbonate platform. In the late Permian (P_2), the Dongwu movement caused crustal extension, and the upper Yangtze region was strongly affected by a high geothermal gradient (60–80 mW·m^{-2}). As a consequence, the Wufeng–Longmaxi shales entered
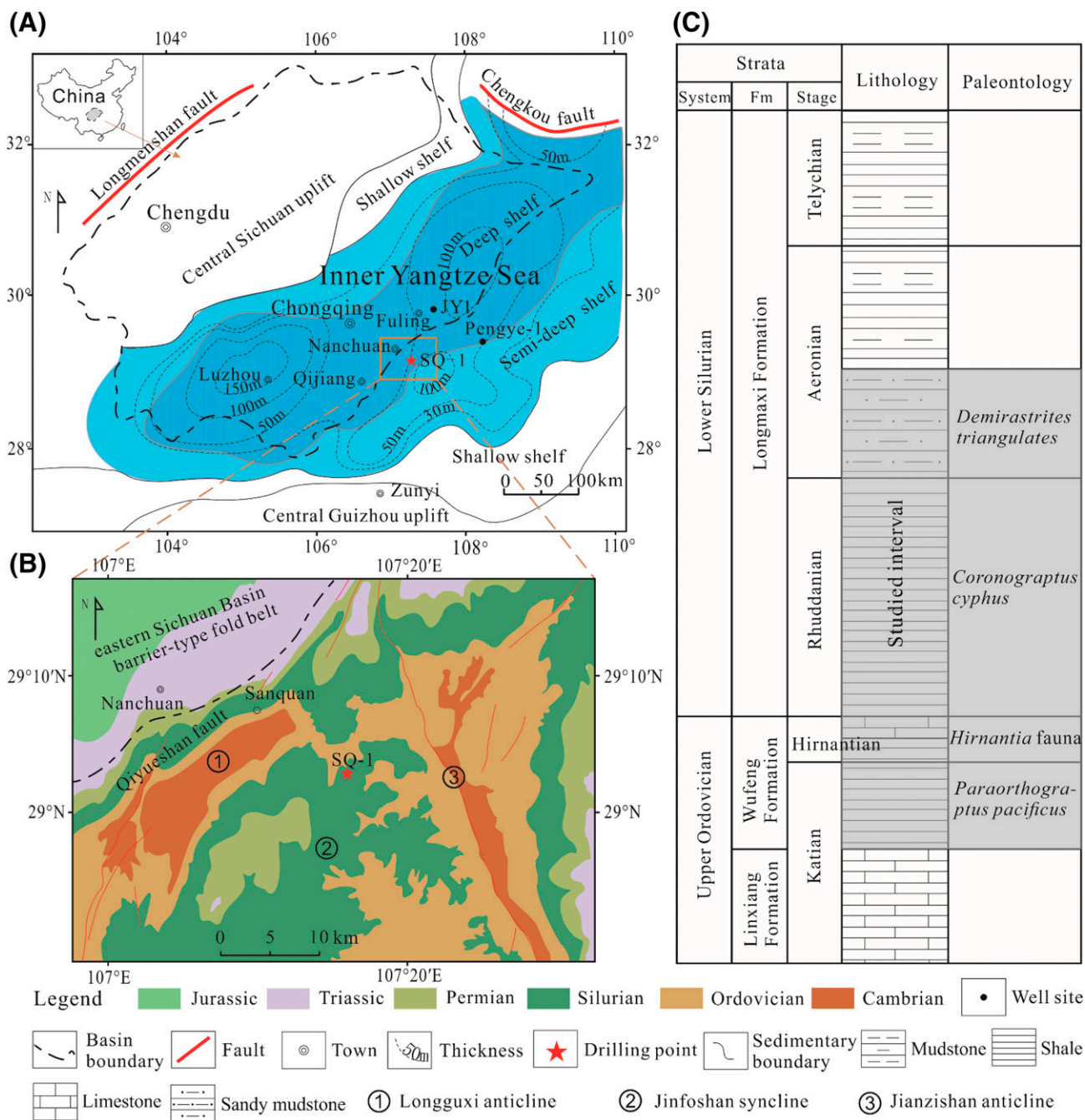
Figure 1. (A) Paleogeographic map of the Sichuan Basin and its neighboring areas during the early Silurian (modified from Chen et al., 2015; Wang et al., 2015b). (B) Regional, geological, and structural profiles of the Sanquan studied area, showing the Sanquan-1 (SQ-1) well and exposed stratum. (C) Stratigraphic column and studied intervals. Fm = Formation; JY1 = Jiaoye 1 well.

the mature stage (Zeng et al., 2011; Nie et al., 2012; Cao et al., 2015b). The burial history of the Longmaxi shales indicates that hydrocarbon generation began in the P₂ and reached the hydrocarbon generation peak between the Late Triassic and Early Jurassic (Zeng et al., 2011; Nie et al., 2012; Guo et al., 2016). In the Early Triassic, the water depth became shallow again,

and evaporite sediments were generally deposited in the upper Yangtze region (Guo, 2014). In the Late Triassic, the upper Yangtze region was quickly buried (Cao et al., 2015b). The area to the east of the Qiyueshan fault reached its maximum depth at circa 145 Ma (early Early Cretaceous), whereas the area west of the Qiyueshan fault reached its maximum

depth at circa 120 Ma (late Early Cretaceous) (Guo and Zhang, 2014).

Since the end of the Early Cretaceous, the area extending from the southeastern margin to the east of the Qiyueshan fault experienced a continuous uplift and superposition by folding (Shen et al., 2007; Guo and Zhang, 2014). As a consequence, compressive fractures or fold-thrust structures occurred extensively at the edge of the basin, such as the area near the Qiyueshan fault (Figure 1B). In the late Yanshan–early Himalayan, the upper Yangtze region that is located to the east of the Qiyueshan fault was affected by the Pacific tectonic system and entered its extension stage, whereas the region located to the west of the Qiyueshan fault was characterized by a compressional uplift and superposition by folding (Shen et al., 2007; Guo, 2014). In the late Himalayan, the entire upper Yangtze region was tectonically uplifted (Cao et al., 2015b; Guo et al., 2016) because of the collision between the Indian plate and the mainland of China (Rowley, 1996). In the late Yanshan–Himalayan, the area from the east of Chongqing to the east of the Qiyueshan fault was denuded, with a total erosion of greater than 4000 m (>13,123 ft) (Yuan et al., 2014).

Sanquan Town is located to the east of the Qiyueshan fault. Outcropping strata include lower Permian, Silurian, Ordovician, and Cambrian units (Figure 1B). Along the southeast margin of the Sichuan Basin, barrier-type folds trend in a northeast direction (Guo and Zhang, 2014), whereas trough-like folds trend in a nearly north–south direction outside of the Sichuan Basin. Therefore, the studied area is located at the transition between the two groups of anticlines and should be within an extensional stress field.

SHALLOW WELL SANQUAN-1 AND SAMPLES

Shallow well Sanquan-1 (SQ-1) was drilled in Sanquan Town of the Nanchuan District, Chongqing Municipality. It is located at the saddle of an anticline close to the northeastern margin of the Jinfoshan syncline. The strata dip 4°. The Longguxi anticline, which trends in a northeast direction, plunges toward the northwest of the SQ-1 well, and the Jianzishan anticline starts to the east of it (Figure 1B). Except for the overlying soil, the real thickness of the shale core is

78 m (256 ft) (Figure 2). No gas show was recorded during drilling.

Core shale samples of both the Upper Ordovician Wufeng Formation and lower part of the lower Silurian Longmaxi Formation were collected from the SQ-1 well (Figure 1C). Core shale samples that were approximately 2.0 cm (~0.8 in.) thick were collected at 0.5-m or 1.0-m (1.6-ft or 3.3-ft) intervals from the bottom up. A total of 101 core samples were selected from the Wufeng Formation and lower Longmaxi Formation.

PRETREATMENT AND METHODS

Geochemical Analysis

Core samples were crushed to approximately 200 mesh and then dried in an oven for 10 hr at 80°C (176°F) before geochemical analyses. The total organic carbon (TOC) values, organic carbon isotopes ($\delta^{13}C$), pyrobitumen reflectance (R_b), mineral compositions, and major elements were measured. Hydrochloric acid (HCl) was used to remove carbonate before the measurement of TOC and $\delta^{13}C$. The powdered shale samples were treated with 5% HCl at 80°C (176°F) for 2 hr, and then they were washed at least six times with deionized water to remove residual HCl. A LECO CS-320 Carbon and Sulfur Analyzer was used for TOC analysis. The detailed analytical procedures are described by Wang et al. (2013). The $\delta^{13}C$ values of 20 treated samples were determined on an elemental analyzer combined with a Thermo DELTA plus XL mass spectrometer. Two replicate measurements were made per sample with an analytical precision of better than ±0.1‰ (Liu et al., 2016).

A 3Y microphotometric system was used to measure pyrobitumen reflectance because of the lack of vitrinite in the Wufeng–Longmaxi shales. When the rock is in a highly overmature stage, the equivalent vitrinite reflectance (R_{equ}) can be obtained using the equation $R_{equ} = (R_b + 0.2443)/1.0495$ (Schoenherr et al., 2007). Optical micrographs of siliceous organisms were also obtained on the 3Y microphotometric system.

An x-ray diffractometer (Olympus Innova-X BTX-II) was used for mineral composition analyses. The diffractometer was equipped with a Co x-ray tube operated at 31 kV and 0.4 mA. The exposure
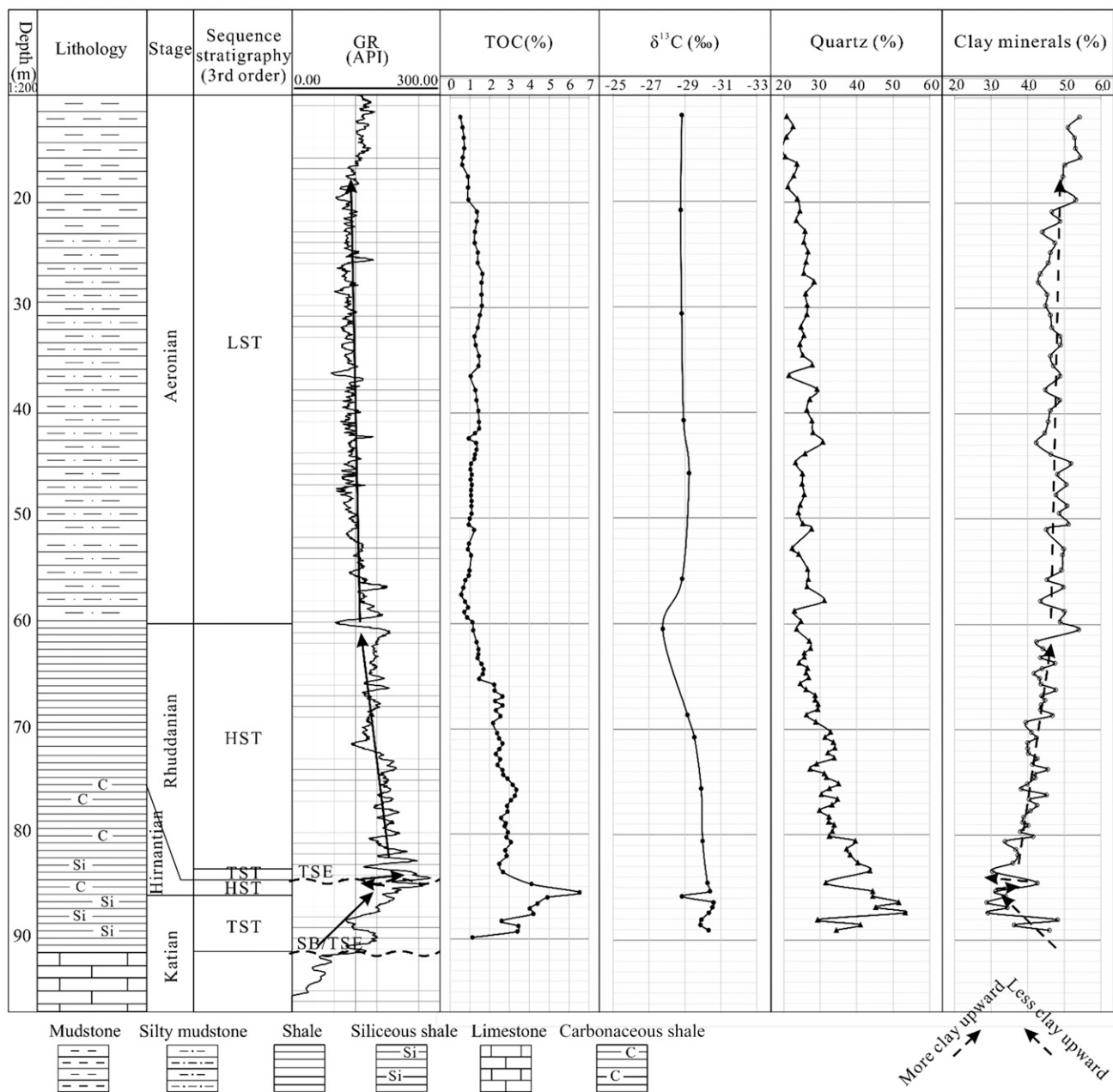
Figure 2. Depth profiles of gamma-ray (GR), total organic carbon content (TOC), $\delta^{13}C$, quartz, and clay contents for the Wufeng–Longmaxi shales, showing lithology and third-order sequence stratigraphy. The dashed lines denote the sequence boundary (SB) or transgressive surface of erosion (TSE). Solid arrows denote variations of API GR counts in a stratigraphic interval, and dashed arrows denote variations of clay minerals in a stratigraphic interval. Siliceous shale is the shale with quartz content greater than 40% and TOC content greater than 2.0 wt. % (Liang et al., 2017). Carbonaceous shale is the shale with TOC content greater than 3.0 wt. % (Liang et al., 2016). HST = highstand systems tract; LST = lowstand systems tract; TST = transgressive systems tract.

time was 70 min, and the exposure rate was three times per minute. Stepwise scanning measurements were performed in the range of 3°–55° (2θ), using a 0.02° (2θ) scanning step. The relative mineral percentages were estimated semiquantitatively using the area under the curve for the major peaks of each mineral.

The mineral compositional result was also semiquantitative (Tian et al., 2013). To improve the understanding of factors that influenced OM accumulation in the shale, the major element concentrations were also investigated. The concentrations of major elements in 15 core samples were determined

by x-ray fluorescence (Rigaku 100e), and the analytical precision of the results was ±3%. One gram of sample was combusted in a muffle oven at 920°C (1688°F) for 4 hr to remove OM and carbonate. Approximately 0.5 g of the ashed sample was mixed with eight times its content of lithium tetraborate ($Li_2B_4O_7$) and fused into glass beads at 1150°C (2102°F) (Li et al., 2017).

Petrophysical Analysis

The total porosity was measured using the MICP techniques that are widely discussed in previous literature (Ross and Bustin, 2009b; Chalmers et al., 2012a; Cao et al., 2015a). The total MICP porosity of the shale samples was measured on a Micrometritics Autopore 9510 Porosimeter. Before MICP porosity analysis, 3–5 g of shale was crushed to 1–20 mesh for each sample and then dried in an oven for at least 24 hr at 110°C (230°F) under vacuum conditions. The initial pressure during the mercury intrusion measurement was set at 0.01 MPa (1.45 psi), and then the pressure was continuously increased to 414 MPa (60,000 psi), which corresponds to a pore size of 3 nm to 120 μm. The total porosities were calculated from the Hg intrusion data (Cao et al., 2015a).

Low-pressure gas adsorption analysis was used to measure the pore-size distribution (PSD) according to N_2 at −195.8°C (−384.4°F) and CO_2 at 0°C (32°F) using an accelerated surface area and porosimetry system (ASAP 2460, Micromeritics Instruments). Approximately 3 g of shale was crushed to 60–120 mesh for each sample and then dried and degassed in a high-vacuum (<10 mm Hg) system for 10 hr at 110°C (230°F). The glass tube containing sample powder was then placed in a −195.8°C (−384.4°F) liquid nitrogen Dewar. The N_2 adsorption of the shale samples at various relative pressures was measured using high-purity N_2 (99.999%) as the adsorbate. The equilibrium interval was 30 s for N_2 and 45 s for CO_2. During the CO_2 adsorption measurements, the free spaces were tested separately and input manually (Wei et al., 2016). The N_2 and CO_2 adsorption isotherms were automatically merged by the instrument.

The FE-SEM imaging of nanopores was performed on shale chips after being treated by argon ion-beam milling (IM4000, Hitachi High-Tech). Secondary electron images for documenting the topographic variation and backscattered electron images to delineate the compositional variation were acquired on both the Hitachi S4800 and Field Electron and Ion Company Helios NanoLab™ 600 systems (Tian et al., 2013).

RESULTS

Sequence Stratigraphy

The sequence stratigraphy and organic geochemistry of shale can be used to identify, predict, and map the target shale interval that has the most potential (Slatt and Rodriguez, 2012; Chen et al., 2015). The drilling logs of the target shale intervals are characterized by high gamma. In general, gamma-ray (GR) values of the SQ-1 well are greater than 130 API, and the maximum value (280 API) occurs near the bottom of the Rhuddanian. In the target shale interval, the TOC content and quartz content have similar varying trends according to GR (Figure 2). At the same time, there is a negative relationship between the API values and clay content. This result is consistent with the result for the Barnett Shale in the north Fort Worth Basin, Texas (Slatt and Rodriguez, 2012).

The Wufeng Formation sits on a sequence boundary (SB) or transgressive surface of erosion (TSE) according to the variation of the lithofacies and GR. Zheng et al. (2013) and Wang et al. (2015a) interpreted the Wufeng Formation as a third-order sequence consisting of a basal SB; lower, upward-increasing API GR transgressive systems tract (TST); and an upper, upward-decreasing API GR highstand or regressive systems tract (HST). The lithofacies of the TST in the Wufeng Formation are mainly composed of black laminated siliceous shale, whereas the HST consists of black carbonaceous shale and 0.3 m (1.0 ft) of calcareous mudstone in the SQ-1 well. The Wufeng Formation shale (84.7–89.6 m [277.9–294.0 ft]) is commonly divided into Katian (86.0–89.6 m [282.2–294.0 ft]) and Hirnantian (84.7–86.0 m [277.9–282.2 ft]). The Katian includes the TST, whereas the HST consists of Hirnantian units (Figure 2).

The Hirnantian is marked by the appearance of the graptolite species *Normalograptus extraordinarius* (Chen et al., 2006), which is accompanied by a positive carbon isotope excursion (CIE) (Chen et al., 2006; Liu et al., 2016) (Figure 2). The lower Silurian

Longmaxi Formation shale is separated from the Upper Ordovician Wufeng Formation shale by the Guanyinqiao calcareous mudstone, which is above the Hirnantian. According to Fan et al. (2011), the lower Longmaxi Formation in the SQ-1 well can be divided into two sections: the lower section (Rhuddanian, 60.5–84.7 m [198.5–277.9 ft]), which consists of black carbonaceous shale with a well-developed horizontal bedding, and the upper section (lower Aeronian, 11.0–60.5 m [36.1–198.5 ft]), which consists of black shale and dark gray silty mudstone. *Demirastrites triangulates*, a biostratigraphic index fossil that is indicative of a variable shallow water body, appeared in the early Aeronian (Fan et al., 2011; Wang et al., 2015a). Therefore, limestone, CIE, calcareous mudstone, and *Demirastrites triangulates* are used to identify the boundaries of the Katian, Hirnantian, Rhuddanian, and lower Aeronian.

Similarly, the Rhuddanian and lower Aeronian (*Demirastrites triangulates*) in the lower Longmaxi Formation constitute another third-order sequence (Chen et al., 2015) that consists of a basal TSE; relatively thin, carbonaceous shale TST; thicker HST; and lower, slightly changing API GR lowstand systems tract (LST). The LST is marked by a falling stage, which exhibits a rapid rate of falling to the relative sea level, and a turnaround stage, which exhibits a slower rate of rise (Slatt and Rodriguez, 2012). The lithofacies of the TST and HST in the lower Longmaxi Formation are composed of black carbonaceous shale and graptolite shale, whereas the LST consists of black shale, silty mudstone, and mudstone (Figure 2). The Rhuddanian includes the TST and HST, and the LST is lower Aeronian (Figure 2).

The Katian–Hirnantian and Rhuddanian in the SQ-1 well are mainly composed of black siliceous shale and carbonaceous shale that are rich in various graptolites and pyrite laminae. Such black carbonaceous shales commonly reflect an anaerobic, deep-water shelf facies. Such a sedimentary environment is commonly considered to be conducive to the enrichment and preservation of OM (Arthur and Sageman, 1994; Strapoć et al., 2010; Liang et al., 2016).

Organic Geochemical Characteristics

The TOC content values in the Katian–Hirnantian, Rhuddanian, and lower Aeronian are in the range of 1.13–6.53 wt. % (average 3.88 wt. %), 1.18–3.34 wt. % (average 2.42 wt. %), and 0.53–1.64 wt. % (average 1.11 wt. %), respectively (Table S1, supplementary material available as AAPG Datashare 98 at www.aapg.org/datashare). Basically, the TOC values of the Wufeng–Longmaxi shales decrease upward in the stratigraphy (Figure 2). The high-quality shale with TOC greater than 2.0 wt. % is approximately 24 m (~79 ft) thick, with an average TOC value of 3.0 wt. %. The OM in the shale samples is mainly composed of amorphous OM and pyrobitumen. The $\delta^{13}C$ values of the bulk OM in the core shale samples are in the range of −30.6‰ to −27.8‰ (Figure 2). Basically, the closer the shale samples to the bottom of the marine shale strata, the lighter the $\delta^{13}C$ values of the bulk OM. In addition, a positive CIE occurs at the bottom of the Hirnantian (Figure 2). Because there is no vitrinite present, the R_{equ} was calculated based on the reflectance of pyrobitumen. Then, R_{equ} was used to designate the stage of hydrocarbon maturation. The R_{equ} values vary in the range of 2.14%–2.76% (Table 1), suggesting that the shales are overmature. Additionally, a few shale samples were also measured according to Rock-Eval 6. The quantities of hydrocarbons that can be potentially released in the sample after maturation (Behar et al., 2001), or S_2 values, are all near zero.

Mineralogy and Major Elemental Characteristics

The x-ray diffraction results indicate that the mineral compositions of the Wufeng–Longmaxi shale samples include quartz, feldspar, calcite, dolomite, pyrite, and clays (illite and chlorite) (Table S1, supplementary material available as AAPG Datashare 98 at www.aapg.org/datashare). A ternary diagram is used to show their mineral compositions (Figure 3). For all 101 samples, the clay contents are in the range of 28.8%–54.3%, with an average of 44.3%. The clay contents in the Katian–Hirnantian, Rhuddanian, and lower Aeronian are in the range of 28.8%–48.1% (average 36.7%), 30.3%–53.9% (average 41.7%), and 42.3%–54.3% (average 48.0%), respectively. Brittle minerals (quartz, feldspar, carbonates, and pyrite) are dominated by quartz (19.6%–53.3%, average 29.0%). The feldspar contents are in the range of 10.6%–21.5%, with an average of 16.4%. The carbonate contents are

Table 1. Lithology and Petrogeochemical Characteristics of the Wufeng–Longmaxi Shales

Sample	Strata	Lithology	TOC (wt. %)	Rock-Eval S_2 (mg HC/g rock)	R_{equ} (%)
SQ-30	Lower Aeronian	Black sandy mudstone	1.51	/	2.15
SQ-45	Lower Aeronian	Black sandy mudstone	1.10	0.01	/
SQ-60	Rhuddanian	Black grapholite shale	1.18	/	2.14
SQ-68	Rhuddanian	Black grapholite shale	2.55	0.01	/
SQ-75	Rhuddanian	Black carbonaceous shale	3.14	0.01	/
SQ-80	Rhuddanian	Black carbonaceous shale	3.07	/	2.56
SQ-84	Rhuddanian	Black siliceous shale	4.11	/	2.26
SQ-85	Hirnantian	Black siliceous shale	6.74	0.05	2.38
SQ-86b	Katian	Black siliceous shale	4.41	/	2.65
SQ-88b	Katian	Black carbonaceous shale	3.45	/	2.76
SQ-89	Katian	Black carbonaceous shale	3.29	0.01	/

Abbreviations: R_{equ} = equivalent vitrinite reflectance; SQ = Sanquan; S_2 = the quantity of hydrocarbons that can be potentially released in the sample after maturation; TOC = total organic carbon.

in the range of 4.4%–14.0%, with an average of 6.8% (Figure 3). The shales in the Hirnantian and Katian have the lowest carbonate contents. They also have low amounts of pyrite.

Except for a few shale samples that are close to the Linxiang Formation limestone, the cumulative contents of quartz, feldspar, and pyrite for most of the Katian–Hirnantian samples are greater than 60%; the Rhuddanian samples are in the range of 50%–65%; and the lower Aeronian samples are approximately 50% (Figure 3). Therefore, there are abundant brittle minerals in the Katian–Hirnantian and Rhuddanian. Brittle minerals are conducive to the formation of natural microfractures and the stimulation of post-fractures by hydraulic fracturing (Jarvie et al., 2007).

The quartz contents in the Katian–Hirnantian, Rhuddanian, and lower Aeronian samples are in the range of 29.3%–53.3% (average 41.7%), 23.5%–43.6% (average 30.9%), and 19.6%–31.3% (average 25.1%), respectively. In general, the quartz content and brittle mineral content of the Wufeng–Longmaxi shales gradually decrease upward in the section, and the maximum quartz content (53.3%) occurs in the Katian (87.6 m [287.4 ft]) (Table S1, supplementary material available as AAPG Datashare 98 at www.aapg.org/datashare). Figure 2 shows that the depth profile of the quartz content is similar to those of the API and TOC. Meanwhile, the quartz contents of the TST and HST are significantly higher than those of the LST system.

Table 2 shows the major oxides of the shale samples. The compositions of the major oxides are highly consistent with the results of the mineral compositions. Basically, SiO_2 is the most abundant of all oxides, ranging from 58.63% to 76.32% (Table 2). Shale samples with a high amount of SiO_2 mainly occur in the Katian–Hirnantian (average SiO_2 = 71.9%), followed by the Rhuddanian (up to 68.6% SiO_2), whereas the silica contents in the shale samples of the lower Aeronian are closer to the average value of the silica contents (58.9%) for various shales (Wedepohl, 1991; Ross and Bustin, 2009a). The shale samples in the Katian–Hirnantian have an average Al_2O_3 content of 7.3%, whereas those in the Rhuddanian and lower Aeronian have average Al_2O_3 contents of 11.6% and 16.3%, respectively. Since the Al_2O_3 contents are related to terrestrial detritus (Wedepohl, 1971; Wang et al., 2014), the variations in the average Al_2O_3 content indicate that the terrestrial detrital input gradually increases from the Katian–Hirnantian to the lower Aeronian.

PETROPHYSICAL PROPERTIES

Mercury Injection Capillary Pressure Porosity

In this paper, the porosity was measured using the MICP method, whereas the pore volume and pore structure were analyzed by nonlocal density functional theory (NLDFT) analysis (Figure 4). The porosities measured by MICP are in the range of 1.8%–6.1% (Figure 4). Except for some samples in the detachment
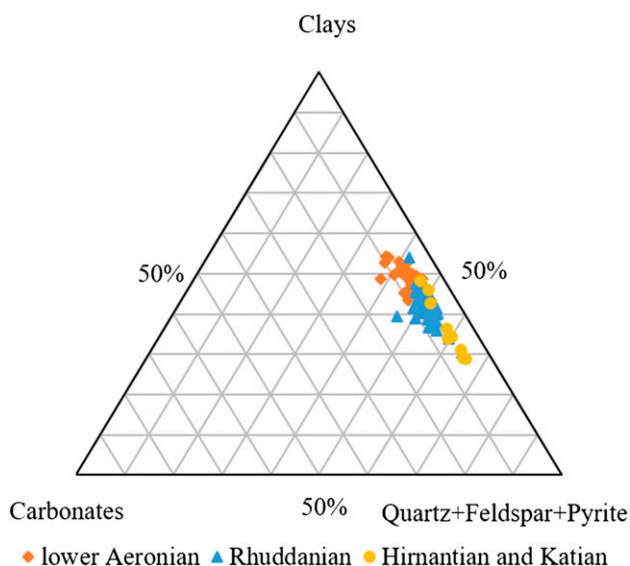
Figure 3. Ternary diagram of the mineralogical compositions of the Wufeng–Longmaxi shales. The carbonate contents of most of the samples are less than 10%. The shales in the Hirnantian and Katian have the lowest carbonate contents. The cumulative contents of quartz, feldspar, and pyrite for most of the Katian–Hirnantian samples are more than 60%; the Rhuddanian samples are in the range of 50%–65%; and the lower Aeronian samples are approximately 50%.

layer and those near the earth surface, the MICP porosities show a good linear relationship with the TOC. Previous research by Jin et al. (2013) suggested that the porosity in black shale near the land surface will increase because of weathering. Basically, the porosities are commonly greater than 3.0% when the TOC values are greater than 2.0 wt. % (Figure 4). The relationship between the pore size and mercury intrusion saturation can also be used to characterize the contribution of pores of various sizes to the porosity of the shales (Cao et al., 2015a). The mercury injection measurement indicates that the Wufeng–Longmaxi shales display a bimodal pattern of PSD because the pore sizes are primarily distributed in the range of 3–50 nm and 30–100 μm (Figure 5). Except for sample SQ-87b, which was collected from the detachment layer, the samples with higher TOC values commonly have more pores in the range of 3–50 nm (mesopore fraction) (Figure 5C). In this study, the following classification of the MICP pore size ranges was used: mesopores (<50 nm) and macropores (50 nm to 120 μm). Figure 4 suggests that mesoporosity (MICP porosity) is dominant, especially for the high-quality shales in the Katian, Hirnantian, and

Rhuddanian, which have TOC values greater than 2.0 wt. %. This result indicates that the organic-rich shales have good pore connectivity because the amount of mercury injected is controlled by the pore throat size (Tang et al., 2015). Additionally, the pore connectivity of the shale in the detachment layer (e.g., SQ-87b) is significantly increased (Figures 4, 5C).

Adsorption Isotherms, Specific Surface Area, and Pore Volumes

When using CO_2 and N_2 gas adsorption methods, the calculation results of the adsorption data may be influenced by both model selection and the accuracy of the parameters (Ross and Bustin, 2009b; Kuila and Prasad, 2013; Tian et al., 2013; Zhang and Yang, 2013; Rouquerol and Rouquerol, 2014; Thommes and Cychosz, 2014; Wei et al., 2016). An accurate depiction of the nanopore structure for organic-rich shale was successfully used by Wei et al. (2016). The NLDFT method can provide a more realistic description of the thermodynamic properties of the fluid in the pores of porous materials (Ravikovitch and Neimark, 2006; Zhang and Yang, 2013; Rouquerol and Rouquerol, 2014; Thommes and Cychosz, 2014). The comparison results from the classical methods, such as the Brunauer–Emmett–Teller, Barrett–Joyner–Halenda, t-plot, and density functional theory methods, and NLDFT method have confirmed that the NLDFT method is a more suitable method for exploring a wide range of pore sizes (0.33–100 nm) for organic-rich shale (Wei et al., 2016).

In this paper, pores were measured using NLDFT analysis based on the CO_2 and N_2 composited adsorption. The pores were classified into three categories according to their pore size: macropores (>50 nm), mesopores (2–50 nm), and micropores (<2 nm) (International Union of Pure and Applied Chemistry, 1994). Additionally, mesopores were further classified into fine mesopores (2–10 nm), medium mesopores (10–25 nm), and coarse mesopores (25–50 nm) (Chalmers et al., 2012a). The isotherm shape of the Hirnantian shale sample (e.g., SQ-85) shows a broad hysteresis at a higher relative pressure (Figure 6C), indicating relatively abundant mesopores (Kuila and Prasad, 2013), whereas the Katian shale sample (e.g., SQ-88b) shows a narrow

Table 2. Major Oxides of the Wufeng–Longmaxi Shales

Sample	Al_2O_3 (%)	CaO (%)	Fe_2O_3 (%)	K_2O (%)	MgO (%)	Na_2O (%)	P_2O_5 (%)	MnO (%)	SiO_2 (%)	SO_3 (%)	TiO_2 (%)	Excess SiO_2 (%)	Ti/Al
SQ-20	15.10	3.44	6.37	3.68	2.41	0.94	0.11	0.03	59.15	3.43	0.72	12.19	0.048
SQ-30	14.57	3.73	6.20	3.54	2.57	0.96	0.08	0.04	58.63	3.30	0.69	13.32	0.047
SQ-45	15.78	2.22	6.26	3.94	2.69	0.83	0.11	0.04	59.94	2.50	0.70	10.86	0.044
SQ-50	15.90	2.03	6.24	4.02	2.78	0.73	0.07	0.04	60.02	2.28	0.68	10.57	0.043
SQ-60	18.02	0.60	4.82	4.92	2.44	0.82	0.11	0.02	61.97	2.09	0.74	5.93	0.041
SQ-65	15.36	2.22	6.41	3.84	2.48	1.20	0.09	0.03	59.15	5.33	0.71	11.38	0.046
SQ-70b	12.39	2.62	6.05	3.13	2.04	0.98	0.11	0.03	62.64	4.80	0.58	24.11	0.047
SQ-75b	12.02	3.42	4.87	3.19	2.04	0.76	0.11	0.03	62.12	3.59	0.59	24.74	0.049
SQ-80b	9.95	2.91	4.13	2.62	1.42	0.67	0.10	0.02	68.64	4.09	0.47	37.70	0.047
SQ-84	11.90	2.07	5.26	3.22	1.66	0.89	0.11	0.02	63.55	6.02	0.58	26.54	0.049
SQ-85	7.74	2.01	3.20	2.10	1.20	0.62	0.10	0.02	70.20	2.68	0.39	46.13	0.050
SQ-86	5.55	2.44	3.03	1.49	1.14	0.39	0.03	0.03	76.19	3.12	0.27	58.93	0.049
SQ-87b	5.72	3.02	2.34	1.50	0.98	0.41	0.06	0.03	76.32	1.08	0.27	58.53	0.047
SQ-88b	8.38	3.73	3.20	2.28	1.68	0.43	0.08	0.05	69.10	1.88	0.40	43.04	0.048
SQ-89b	15.65	3.56	4.36	4.21	2.93	0.92	0.08	0.05	56.82	1.55	0.76	8.15	0.049

Abbreviations: SQ = Sanquan; Ti/Al = TiO_2/Al_2O_3.

hysteresis (Figure 6D), indicating that the Katian shales have fewer mesopores but more macropores than those of the Hirnantian. Furthermore, the shales in both the Katian and the Hirnantian have similar absorbed gas quantities at high relative pressure ($P/P_o = 0.995$; the ratio of adsorption gas pressure [P] to saturation pressure [P_o]), indicating that the shale samples with different TOCs have similar total pore volumes. However, the Rhuddanian and lower Aeronian shale samples (Figures 6A, B) show no significant differences in isotherm shape. As a whole, the adsorbed volume of the shale samples is positively related to the TOC, whereas the samples in the detachment layer have abnormally high numbers of macropores (Figures 4, 6).

The specific surface area and pore volume of the shale samples calculated from the adsorption isotherms using the NLDFT method are shown in Table 3. The total specific surface area (S_{total}) values of the samples in the Katian–Hirnantian, Rhuddanian, and lower Aeronian are in the ranges of 26.5–42.0 m^2/g (average 31.2 m^2/g), 19.3–32.8 m^2/g (average 24.8 m^2/g), and 16.1–19.9 m^2/g (average 18.5 m^2/g), respectively, decreasing upward (Figure 4). Similarly, the total pore volume (V_{total}) values of the Katian–Hirnantian, Rhuddanian, and lower Aeronian are in the ranges of 30.6–41.4 ×10^{-3} cm^3/g (average 37.6 ×10^{-3} cm^3/g),

23.0–32.3 ×10^{-3} cm^3/g (average 26.8 ×10^{-3} cm^3/g), and 20.1–24.3×10^{-3} cm^3/g (average 22.6×10^{-3} cm^3/g), respectively. Furthermore, both S_{total} and V_{total} show positive relationships with the TOC (Figures 4, 7D). Basically, when the TOC values of the shale samples are greater than 2 wt. %, the S_{total} values are commonly greater than 24.0 m^2/g, and the V_{total} values are commonly greater than 23.0 ×10^{-3} cm^3/g (Figures 4, 7D). Therefore, nanopores formed by hydrocarbon generation and expulsion should have greatly contributed to the increase in the specific surface area and pore volume, as well as the porosity.

As shown in Figure 4 and Table 3, S_{total} is dominated by the micropore specific surface area, and V_{total} is dominated by the mesopore volume. In addition, V_{total} values of the samples in the detachment layer are higher (20%–27%) than those of the other shale samples with similar TOC values (Figures 4, 7D).

Pore-Size Distributions of the Shale Samples

The parameter $dV/d(\log[D])$ (partial volume V of each pore diameter D) is widely used to display the distribution of the mesopore and macropore volume because the visual area under the curve between any two pore diameters of $dV/d(\log[D])$ is considered to be proportional to the real pore volume (Clarkson

Figure 4. Depth profiles of the nonlocal density functional theory (NLDFT) specific surface area, NLDFT pore volume, and mercury injection capillary pressure (MICP) porosity for the Wufeng–Longmaxi shales. The detachment layer (86.9–88.5 m [285.1–290.4 ft]) is shown in green. The blue dashed line and red solid line denote the overall trends of the macroporosity (50 nm to 120 μm) and mesoporosity (<50 nm) measured using the high-pressure Hg porosimetry. The varying trends of the petrophysical properties of the Wufeng–Longmaxi shales are similar to that of the total organic carbon (TOC) content to some extent. However, the macroporosity of sample SQ-85 (85.4 m [280.2 ft]) is decreased significantly, whereas the mesoporosity of sample SQ-87b (87.4 m [286.7 ft]) in the detachment layer is increased significantly. SQ = Sanquan.
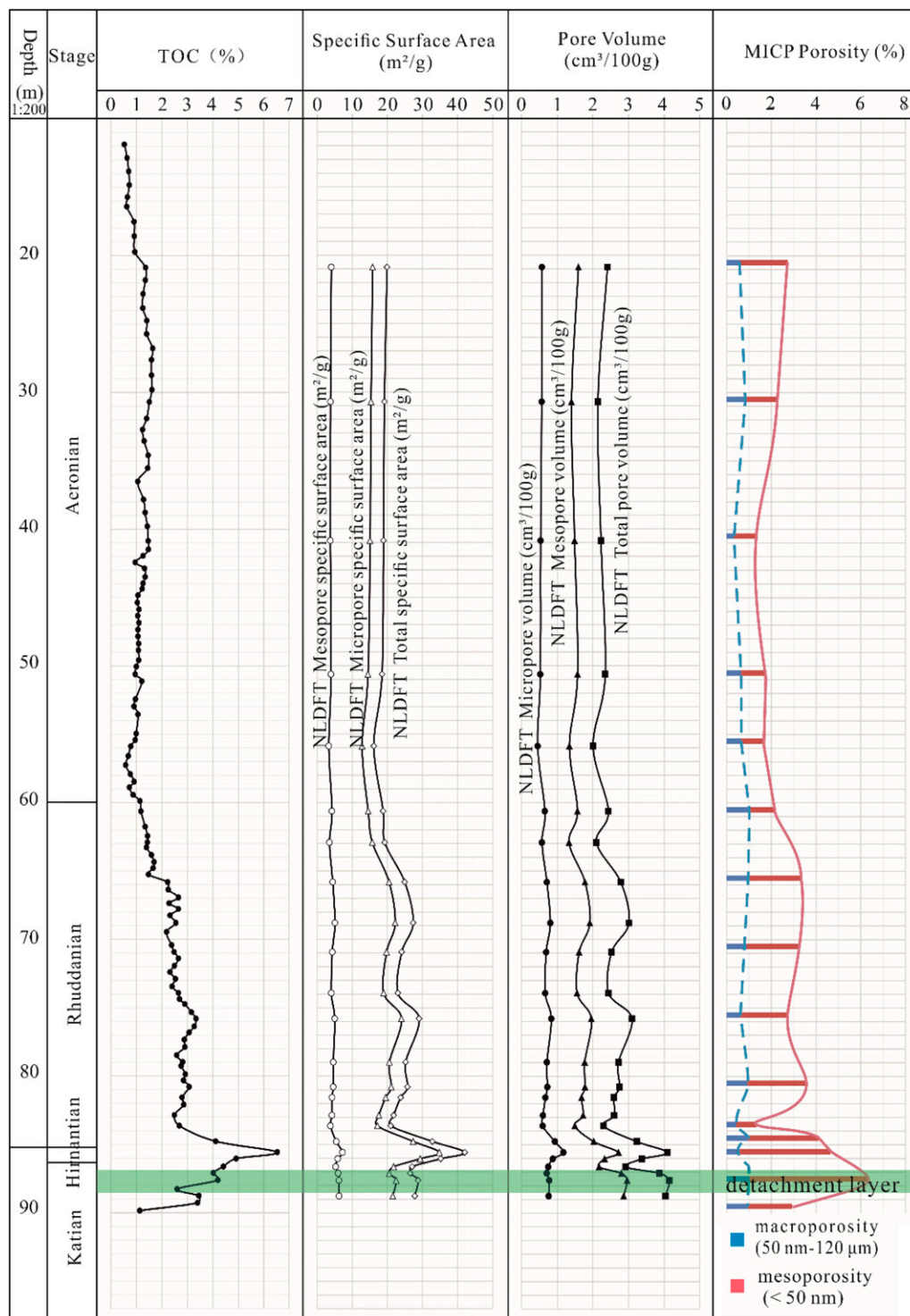
et al., 2012; Kuila and Prasarad, 2013; Tian et. al., 2013). Figure 8 shows the PSDs of the Wufeng–Longmaxi shales using the application of the Barrett–Joyner–Halenda method, assuming Harkins–Jura's thickness equation model, which were calculated based on the N$_2$ adsorption branch of the isotherms.

The PSDs of the shale samples from the lower Aeronian are similar to each other but slightly different from those of the Rhuddanian and significantly different from those of the Hirnantian and Katian (Figure 8). The shales from the Katian and Hirnantian are characterized by a relatively high abundance of

mesopores in the total pore volume. Most samples show a unimodal peak at approximately 10–50 nm (Figure 8C). When the TOC is greater than or equal to 4.1 wt. %, the pore size less than 25 nm increases as the TOC increases, whereas the pore size greater than or equal to 25 nm decreases as the TOC increases (Figure 8B, C). Although samples SQ-86b and SQ-87b have similar TOC and clay contents (Figure 8C), the pores of the SQ-87b are obviously more abundant than those of SQ-86b, especially when the pore size is greater than 10 nm. This indicates that the microcracks in the detachment layer can connect more pores and improve the connectivity of the shale.

Field Emission Scanning Electron Microscopy of Shales

After being processed by Ar ion-beam milling, the nature of the pore system of the core samples was studied using FE-SEM. The previous literature revealed that OM grains are either a mixture of kerogen, clay, and carbonate (Chalmers et al., 2012a) or pyrobitumen (Bernard et al., 2012; Loucks and Reed, 2014). A mass of microfossils, such as sponge spicules and radiolarians (Figure 9A, B), was observed in the siliceous shales with a high TOC that mainly occurs in the Katian. The Wufeng–Longmaxi shales commonly contain a complex porous system that includes pores, pore throats, and cracks.

Figure 10 shows the details of the Rhuddanian shale (e.g., SQ-80b) under FE-SEM. The darker materials are OM grains under FE-SEM (Figure 10A). Most of the OM grains occur in aggregates of authigenic microcrystalline quartz (Figure 10A). In this porous system, various types of pores are associated with OM grains (Figure 10B). Under FE-SEM imaging, OM grains can be classified into two types: migrated OM (pyrobitumen) (Figure 10B) and depositional OM (kerogen) (Figure 10C, D) (Loucks and Reed, 2014; Zhao et al., 2017). Kerogen is commonly in direct contact with the detrital mineral grains (Bernard et al., 2012; Loucks and Reed, 2014). Because of mechanical compaction, kerogen was observed not only along the detrital mineral grain boundaries (Figure 10C, D) but also in the primary interparticle mineral pores (Figure 10A). Kerogen around feldspar seems to lack observable pores under

FE-SEM (Figure 10D). Because of high TOC values, the Wufeng–Longmaxi shales should have generated considerable amounts of liquid hydrocarbons, which may crack during later thermal maturation, resulting in many nanopores. Pyrobitumen in the Wufeng–Longmaxi shales is rich in various types of mesopores and macropores (Figure 10B), which may be because of protection that was provided by rigid authigenic quartz grains. Additionally, because the resolution of the FE-SEM images was approximately 5 nm, micropores (<2 nm) were barely detectable by FE-SEM in pyrobitumen and kerogen. In fact, it is very difficult to strictly differentiate kerogen OM grains from pyrobitumen OM grains under FE-SEM because most of the original OM in the Wufeng–Longmaxi shale are amorphous macerals.

Compared with the Rhuddanian shale, a more complex pore system occurs in the Hirnantian shale sample (Figure 11). More abundant OM grains are present among the detrital quartz, which is consistent with the fact that the average TOC content of the Hirnantian shale is higher than that of the Rhuddanian shale. Kerogen that is in direct contact with detrital quartz seems to be rich in mesopores (Figure 11A, B). Similar to the Rhuddanian shale, pyrobitumen among authigenic quartz is also rich in various types of mesopores and macropores (Figure 11B). A primary intraparticle mineral pore is fully filled with OM grains, which contain many devolatilization microcracks (Figure 11C, D). Devolatilization microcracks occur in bitumen and pyrobitumen or the boundary between OM and minerals (Loucks and Reed, 2014). Kerogen can generate bitumen. Bitumen can evolve into solid bitumen (accompanied by devolatilization microcracks) and then into pyrobitumen during thermal maturation (Loucks and Reed, 2014). It is difficult for OM grains to preserve macropores and coarse mesopores when the protection of authigenic quartz grains is absent in this semiclosed intraparticle mineral pore (Figure 11D).

As shown in Figure 11E, there is a fracture through the OM aggregate that is a part of the pore network. Despite whether the fractures were formed during tectonic movements or not, during or after coring, they are important indicators of whether natural microfractures and postfractures by hydraulic fracturing can be formed (Jarvie et al., 2007; Loucks and Reed, 2014). Because some fractures were partially filled with carbonate (Figure 11F), the fractures are likely to

Figure 5. Pore-size distribution that was defined by the pore volume from porosimetry analysis using the high-pressure Hg porosimetry. The pore diameters range between 3 nm and 120 μm. Bold dashed lines denote the boundaries between micropores (<2 nm), mesopores (2–50 nm), and macropores (>50 nm). (A) The lower Aeronian, (B) the Rhuddanian, and (C) the Katian–Hirnantian. SQ = Sanquan; TOC = total organic carbon.
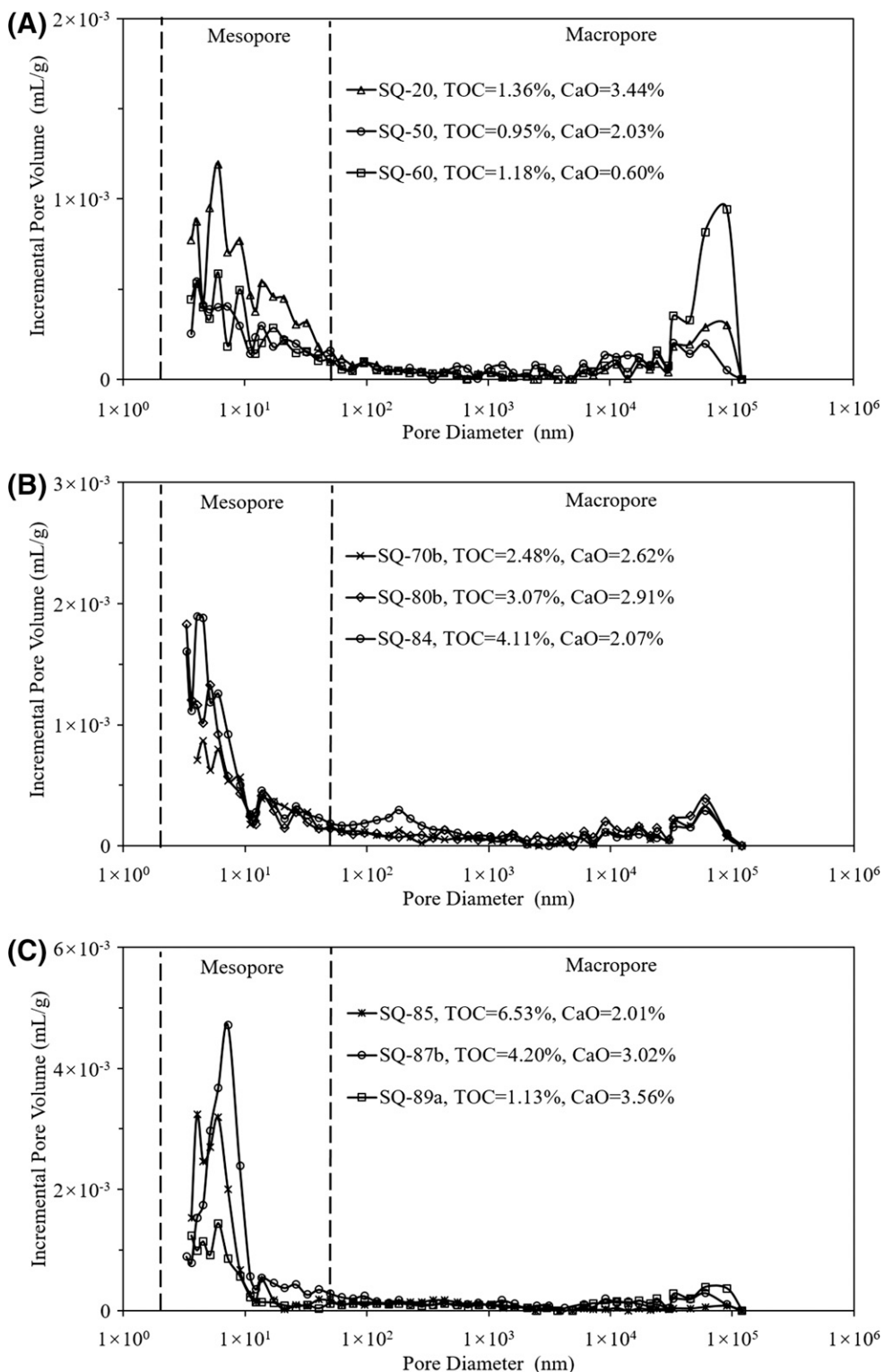
be natural microcracks (e.g., tectonic microcracks and devolatilization microcracks). Tectonic microcracks occur along the arrangement direction of quartz and feldspar and extend far greater than 20 μm along the laminae (Figure 11E).

Figure 12 shows that the Katian shale sample contains a complex porous system that includes organic pores, clay mineral intraparticle pores, intercrystalline pores in graptolites, intergranular pores in pyrite, framboids, and microcracks (Figure
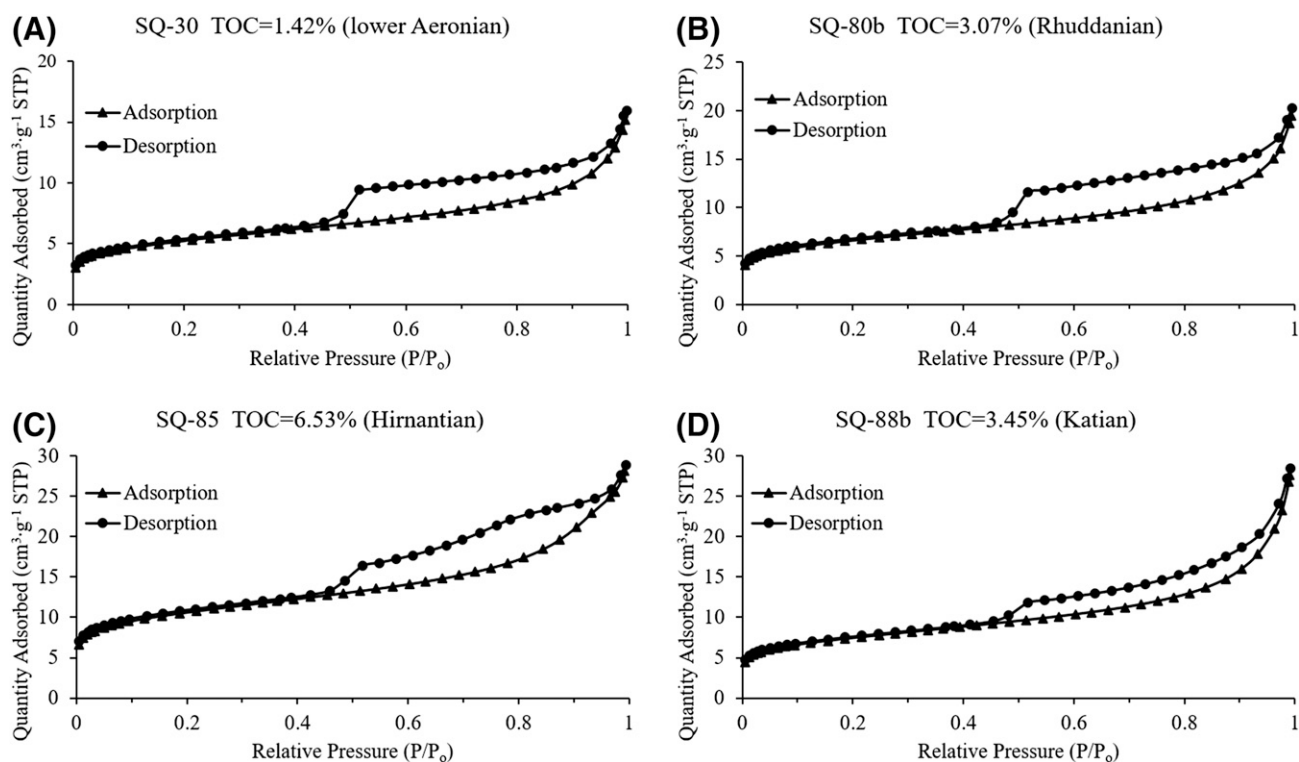
Figure 6. Nitrogen gas adsorption and desorption isotherms of the Wufeng–Longmaxi shales. (A) The lower Aeronian, (B) the Rhuddanian, (C) the Hirnantian, and (D) the Katian. SQ = Sanquan; STP = Standards Technical Panel; TOC = total organic carbon.

12). Different from the images of the shales in the Hirnantian, there are more microcracks in the Katian. It seems that the pore system and mineral shape in the Katian experienced compression and shearing deformation during tectonic movements. As a consequence, detachment layer and interlayer slip scratches occur extensively in the Katian (Figure 13), resulting in microcracks (Figure 12A) and twisting of the original orientations of mineral particles (Figure 12C, D). In fact, Figure 8C indicates that there are more macropores and coarse mesopores in the Katian shale samples near the detachment layer (i.e., SQ-87b and SQ-88b) than in both the Hirnantian and Rhuddanian. Furthermore, pyrobitumen occurs extensively in the pore space between minerals in the Katian, Hirnantian, and Rhuddanian.

DISCUSSION

The above results from Sanquan indicate that high-quality shales mainly occur in the Katian and Hirnantian of the Wufeng Formation and also in the Rhuddanian of the Longmaxi Formation. These shales have relatively high TOC contents and an excellent OM type. The previous literature mentioned that the organic types of the Wufeng–Longmaxi shale are mainly type I and type II (i.e., Liang et al., 2014). This is consistent with our above maceral compositional results and the $\delta^{13}C$ values of the bulk OM. The previous literature also revealed that the Wufeng–Longmaxi shales have a considerable commercial value and can be 40–50 m (131–164 ft) thick (Guo and Liu, 2013; Guo and Zhang, 2014; Guo et al., 2014a). However, high-quality shales do not occur in the lower Aeronian of the Longmaxi Formation.

The brittle mineral contents, especially quartz, decrease upward. The quartz contents in the Katian, Hirnantian, and Rhuddanian are significantly higher than those of the lower Aeronian shales. In the studied area, the lithology of the Katian, Hirnantian, and Rhuddanian mainly includes siliceous shale and carbonaceous shale in the TST and HST, whereas the lower Aeronian is dark gray mudstone and silty mudstone in the LST. Thus, the shale gas resource potential and exploitability of the shales deposited in the TST and HST seem to be better than those deposited in the LST. In the Hirnantian, the detrital

Table 3. Pore Structure Parameters Obtained by the Nonlocal Density Functional Theory Method

	Composited N_2 and CO_2 NLDFT Model							
	Surface Areas (m^2/g)				Pore Volumes (10^{-3} mL/g)			
Sample	S_{mic}	S_{mes}	S_{mac}	S_{total}	V_{mic}	V_{mes}	V_{mac}	V_{total}
SQ-20	15.82	4.01	0.07	19.9	5.68	15.94	2.48	24.10
SQ-30	15.33	3.78	0.04	19.2	5.62	14.01	1.76	21.39
SQ-40	15.06	3.75	0.05	18.9	5.34	14.88	2.05	22.27
SQ-50	14.47	3.92	0.08	18.5	5.25	15.70	2.52	23.47
SQ-55	12.78	3.30	0.05	16.1	4.50	13.42	2.14	20.06
SQ-60	14.52	4.19	0.07	18.8	6.52	15.67	2.15	24.34
SQ-62b	15.70	3.49	0.06	19.3	5.71	13.31	1.98	21.00
SQ-65b	20.48	4.39	0.07	24.9	7.08	17.80	2.95	27.83
SQ-68b	22.24	5.04	0.07	27.4	8.05	19.15	2.91	30.11
SQ-70b	19.77	4.27	0.06	24.1	6.89	16.14	2.22	25.25
SQ-73b	18.94	4.01	0.06	23.0	6.64	15.57	2.20	24.41
SQ-75b	24.02	4.97	0.08	29.1	8.32	19.58	3.06	30.96
SQ-78b	20.58	4.57	0.06	25.2	7.09	17.72	2.38	27.19
SQ-80b	21.11	4.55	0.06	25.7	7.21	17.78	2.47	27.46
SQ-81	19.50	4.22	0.06	23.8	6.68	16.81	2.40	25.89
SQ-82b	17.56	4.16	0.07	21.8	6.00	17.23	2.75	25.98
SQ-83	17.13	3.76	0.05	20.9	5.89	14.91	2.18	22.98
SQ-84	27.36	5.39	0.07	32.8	9.33	20.23	2.74	32.30
SQ-85	34.81	7.19	0.05	42.0	11.68	27.17	2.07	40.92
SQ-86a	29.35	5.82	0.04	35.2	8.74	23.27	1.76	33.77
SQ-86b	21.78	5.20	0.03	27.0	7.45	21.70	1.40	30.55
SQ-87a	20.48	5.91	0.09	26.5	7.09	28.07	3.60	38.76
SQ-87b	22.47	6.15	0.10	28.7	7.73	29.59	4.10	41.42
SQ-88b	21.54	6.17	0.11	27.8	7.56	28.61	4.16	40.33

$1 \text{ cm}^3/\text{g} = 1 \text{ ml/g}$.

Abbreviations: NLDFT = nonlocal density functional theory; S_{mac} = the macropore specific surface area; S_{mes} = the mesopore specific surface area; S_{mic} = the micropore specific surface area; $S_{total} = S_{mic} + S_{mes} + S_{mac}$; SQ = Sanquan; V_{mac} = the macropore volume; V_{mes} = the mesopore volume; V_{mic} = the micropore volume; $V_{total} = V_{mic} + V_{mes} + V_{mac}$.

shales may have a biogenic origin (Chalmers et al., 2012b). Furthermore, the abundant radiolarians and graptolites in the Katian shales can provide additional evidence. Siliceous ooze with an opal mineralogy will transform to microcrystalline aggregates of quartz during diagenetic processes (Schieber et al., 2000; Zhao et al., 2017). Therefore, the main morphology of the siliceous organisms in shale will occur as authigenic quartz. Furthermore, the brittleness of the shale in the TST and HST is largely increased as the content of authigenic quartz increases.

Based on the composition of the major oxides shown in Table 2, the excess silica content in each sample can be calculated using the formula below (Ross and Bustin, 2009a; Wang et al., 2014; Zhao et al., 2017). The average value of $(Si/Al)_{background}$ for shales is typically set at 3.11 (Wedepohl, 1971; Ross and Bustin, 2009a; Wang et al., 2014; Zhao et al., 2017).

$$Si_{excess} = Si_{sample} - \left[(Si/Al)_{background} \times Al_{sample} \right]$$

Table 2 indicates that the excess silica content decreases upward from the Katian–Hirnantian (43.0%–58.5%) to the Rhuddanian (24.1%–37.7%) to the lower Aeronian (5.9%–12.2%). Previous research indicated that excess silica in mudstone and shale can be mainly derived from coarser-grained detrital sediments, clay mineral diagenesis, and siliceous ooze (i.e., diatoms, radiolarians, silicoflagellates, and sponges) (Caplan and Bustin, 1998; Schieber et al., 2000; Ross and Bustin, 2008; Peltonen et al., 2009; Zhao et al., 2017). Here the genesis of excess silica is explored using indices. The Ti/Al ratio (TiO_2/Al_2O_3) is considered to be an indicator of the sedimentation rate (Murphy et al., 2000; Rimmer et al., 2004). A positive relationship between Ti/Al and TOC was reported by Rimmer et al. (2004). An increase in organic productivity is commonly attributed to an elevated nutrient supply (Xu et al., 2017) caused by either the enhanced physical and chemical weathering on the continents (Liu et al., 2016) or an increase in the upwelling current (Liang et al., 2016). The Ti/Al ratios of the shale samples are high and almost constant (0.048 ± 0.001) from 70.5 to 89.6 m (231.3 to 294.0 ft), which corresponds to the shales from the Katian to the lower Rhuddanian (Table 2). Therefore, excess silica was mainly deposited at the high Ti/Al stage (Figure 15A).

Furthermore, the excess silica content has a strong linear relationship with the TOC, and the
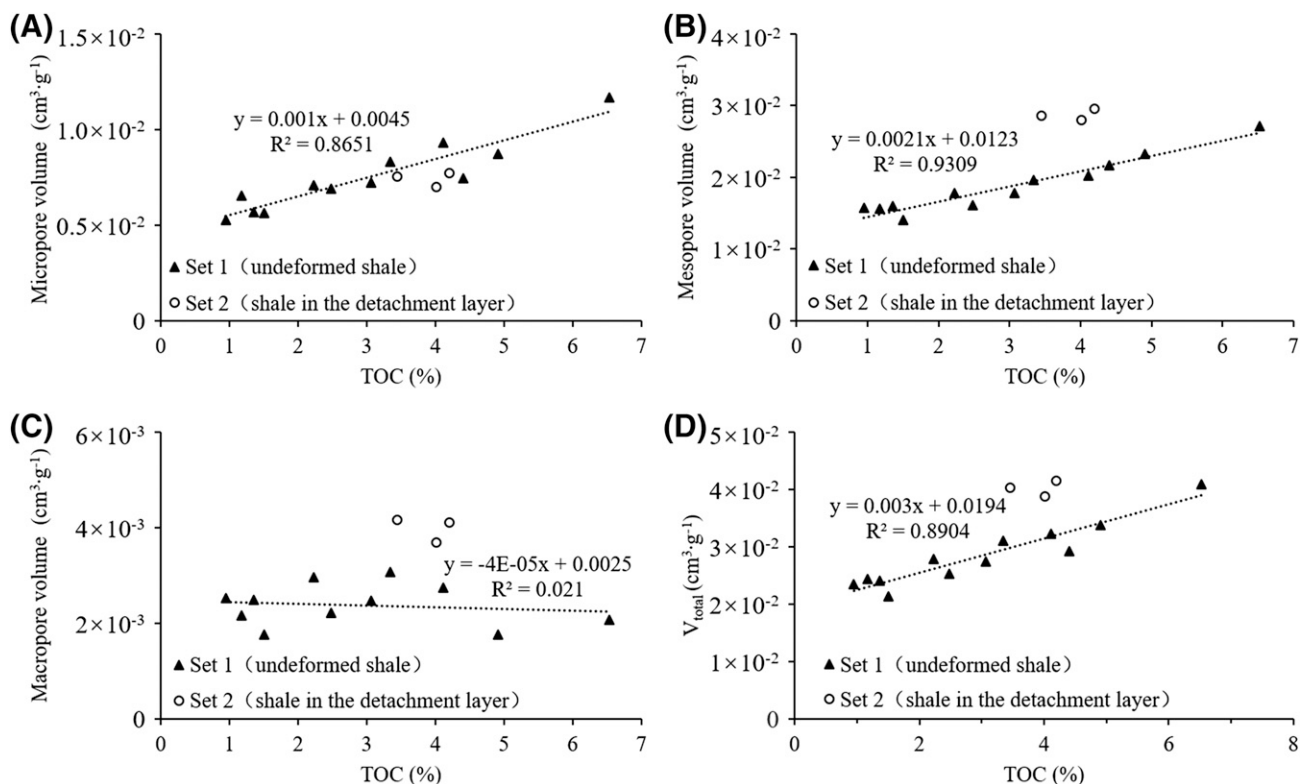
quartz particles show good gradation and fine roundness (Figure 11A, C), which may be attributed to the Hirnantian glaciation that caused the sea level to drop 70–100 m (230–328 ft) (Brenchley et al., 2003; Finnegan et al., 2011; Liu et al., 2016). Therefore, the well-sorted sand in the coastal zone could be transported a long distance to the deeper water body before being deposited on the seafloor.

The positive relationship between the quartz content and TOC (Figure 14) indicates that a part of the quartz in the Rhuddanian, Hirnantian, and Katian

Figure 7. The relationship between the pore volume (measured the adsorption of the N_2 and CO_2) and total organic carbon (TOC). (A) The relationship between the micropore volume (V_{mic}) and TOC. (B) The relationship between the mesopore volume (V_{mes}) and TOC. The micropores and mesopores are mainly related to the TOC. (C) The relationship between the macropore volume (V_{mac}) and TOC. (D) The relationship between the total pore volume (V_{total}) and TOC. R^2 = coefficient of determination; $V_{total} = V_{mic} + V_{mes} + V_{mac}$.

trend line almost passes through the origin (Figure 15B), providing additional evidence that the gradual increase in excess silica of the shales from the Rhuddanian, Hirnantian, and Katian should be attributed to the gradual increase in the biogenic quartz content. The results from cathodoluminescence scanning electron microscopy and major elements analyses also provide evidence that the excess silica in the Wufeng–Longmaxi shales is biogenic (Zhao et al., 2017). This type of authigenic quartz crystal is 1–3 μm and is characterized by irregular microcrystalline aggregates, which are distributed among the detrital quartz (subrounded, 5–20 μm) (Zhao et al., 2017). Abundant microcrystalline aggregates of authigenic quartz are present in the Katian and Rhuddanian (Figure 9D).

The petrophysical properties (MICP porosity, specific surface area, pore volume, and PSDs) of the Wufeng–Longmaxi shales are positively related to the TOC in that higher TOC shales commonly have a higher porosity, pore volume, and specific surface

area. The development and distribution of OM pores depend on the OM types (Loucks and Reed, 2014; Zhao et al., 2017). The OM grains seem to have a significant influence on the porosity and pore volume because OM grains, especially pyrobitumen (Bernard et al., 2012; Loucks and Reed, 2014), can develop various scales of pores (Figures 10–12). Many nanopores can form within kerogen during hydrocarbon generation and expulsion (Jarvie et. al., 2007; Chalmers et al., 2012a). Furthermore, nanopores could also be formed during bitumen secondary cracking (Bernard et al., 2012; Loucks and Reed, 2014), as is supported by FE-SEM imaging (Figures 10B, 11B, D, F, 12B). Therefore, nanopores related to OM should have greatly contributed to the porosity of the Wufeng–Longmaxi shales, especially for samples with high TOC values. However, there is no relationship between the macropore (50–100 nm) volume and TOC (Figure 7C). Especially for samples with a TOC greater than 4.1 wt. %, there is no increase in the macropore volume as the

Figure 8. Pore volume distribution using the application of the Barrett–Joyner–Halenda method, assuming Harkins–Jura's thickness equation model. (A) The lower Aeronian, (B) the Rhuddanian, and (C) the Katian–Hirnantian. Dashed lines denote the shale samples in the detachment layer. dV/dlog(D) = partial volume (V) of each pore diameter (D); SQ = Sanquan; TOC = total organic carbon.
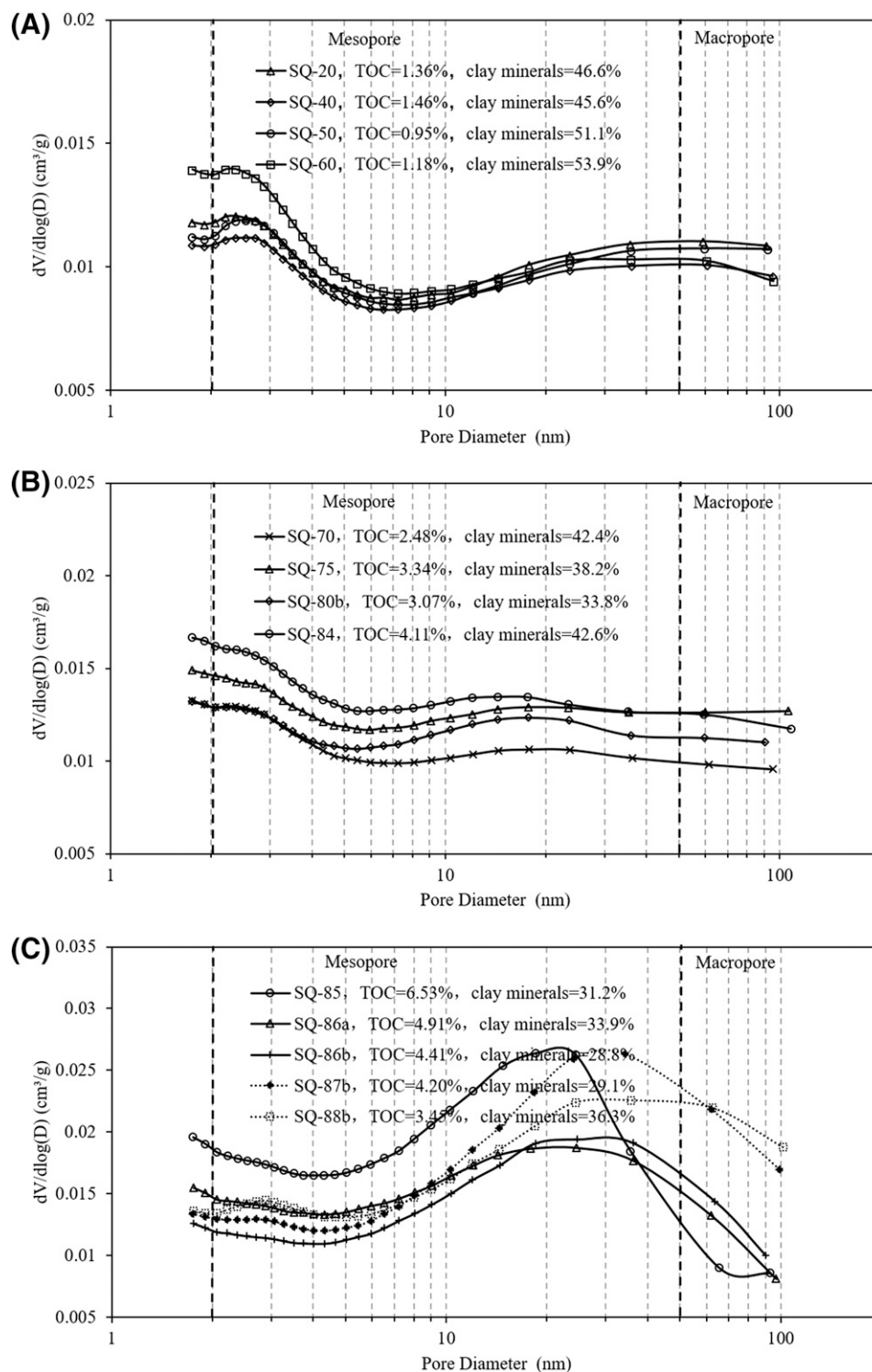
TOC increases (Figure 7C). The Devonian Marcellus Shale was reported to have similar relationships with the macropore volume and variations in the TOC (Mastalerz at al., 2013).

Furthermore, the PSDs of the shale samples in the Katian may be affected by tectonic movements (dotted lines, Figure 8C). Deformation phenomena, such as fault mirrors, scratches, and microfolds (Guo and Zhang, 2014), occur extensively in the detachment layer at the bottom of the Wufeng–Longmaxi Formations (Yan et al., 2003; Guo and Zhang, 2014; Wang et al., 2015c). The previous
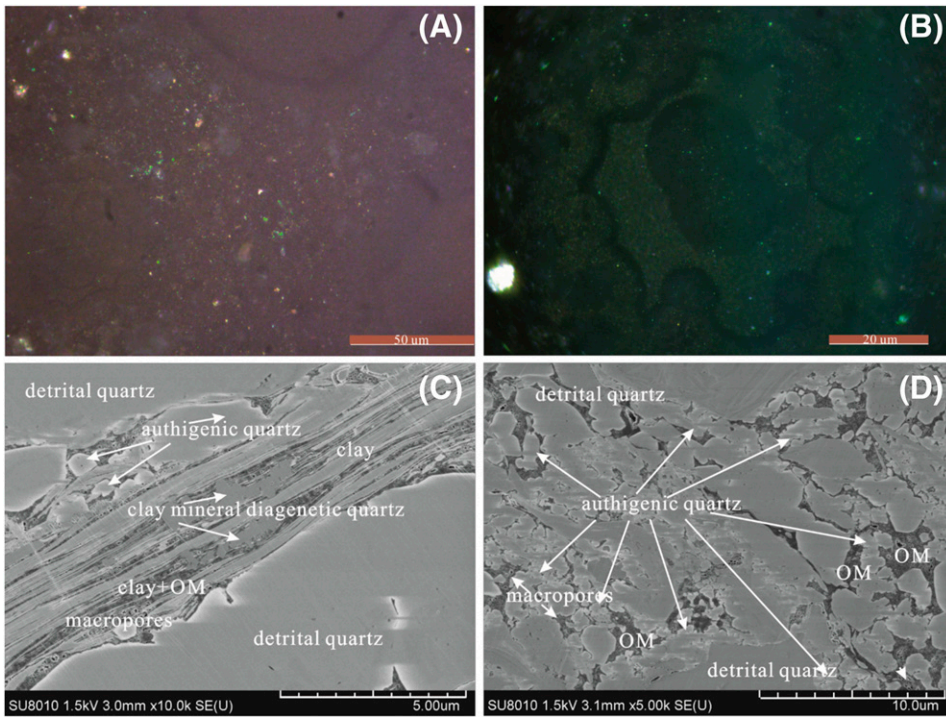
2256   Characteristics of the Wufeng–Longmaxi Shales in Sanquan, Nanchuan of Chongqing

Figure 9. The field emission scanning electron microscopy (FE-SEM) photomicrographs of some shale samples. (A, B) Optical micrographs (3Y microphotometric system) of siliceous organisms in the siliceous shale, 88.6 m (290.7 ft). (C) The FE-SEM photomicrograph of clay mineral diagenetic quartz in the clay, 80.4 m (263.8 ft). Diagenetic quartz from the clay minerals is only responsible for a small part of authigenic quartz. (D) The FE-SEM photomicrograph of authigenic quartz (1–3 μm) among the detrital quartz (5–20 μm), 86.8 m (284.8 ft). Siliceous shale is the shale with quartz content greater than 40% and total organic carbon content greater than 2.0 wt. % (Liang et al., 2017). OM = organic matter.

literature reported that such detachment layers are commonly observed in the Wufeng–Longmaxi Formations of South China (Yan et al., 2003; Guo and Zeng, 2015; Liang et al., 2017). Figure 13 shows that there are interlayer slip scratches on the shale core cross sections of the Wufeng Formation, indicating that the shale experienced a severe tectonic deformation.

The coarse mesopore and macropore volumes of the shale samples in the Katian were significantly higher in the detachment layer. We believe that the
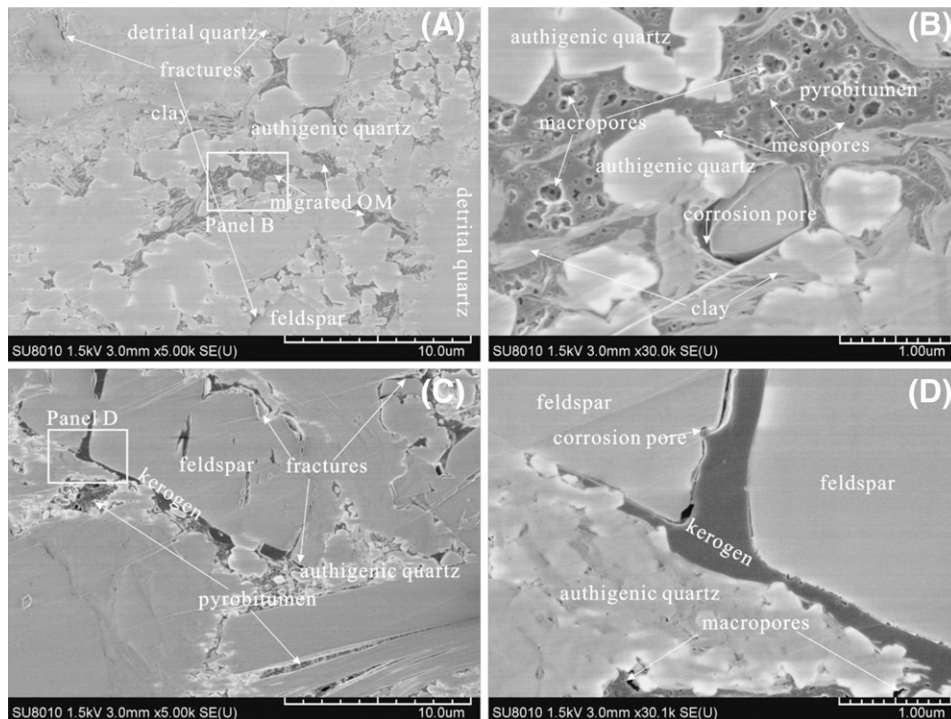

Figure 10. The field emission scanning electron microscopy (FE-SEM) images of the Rhuddanian sample, 80.4 m (263.8 ft). (A) Migrated organic matter (OM) (pyrobitumen) occurs in the aggregates of authigenic microcrystalline quartz. (B) Pyrobitumen with a well-developed spongy texture, containing many OM pores. (C) The FE-SEM photomicrograph of depositional OM (kerogen) shows no crystal growth between it and adjacent minerals. Kerogen was squeezed around feldspar, eliminating most of the visible primary intraparticle mineral pores. (D) Kerogen grains lack observable pores.

Figure 11. The field emission scanning electron microscopy (FE-SEM) images of the Hirnantian sample, 85.6 m (280.8 ft). (A) Abundant kerogen filling among the detrital quartz grains. (B) Kerogen grains in direct contact with the detrital quartz grains containing many mesopores and pyrobitumen among authigenic quartz grains containing various types of mesopores and macropores. (C, D) The FE-SEM photomicrographs of a semiclosed primary intraparticle mineral pore that was filled with organic matter (OM) and devolatilization microcracks. (E) Fractures occur along the arrangement direction of quartz and feldspar. They are commonly aligned parallel to laminae (white dashed lines). (F) A fracture through OM aggregate generating a better connection in the pore networks of shale. Fracture between the OM and quartz is partially filled with carbonate.
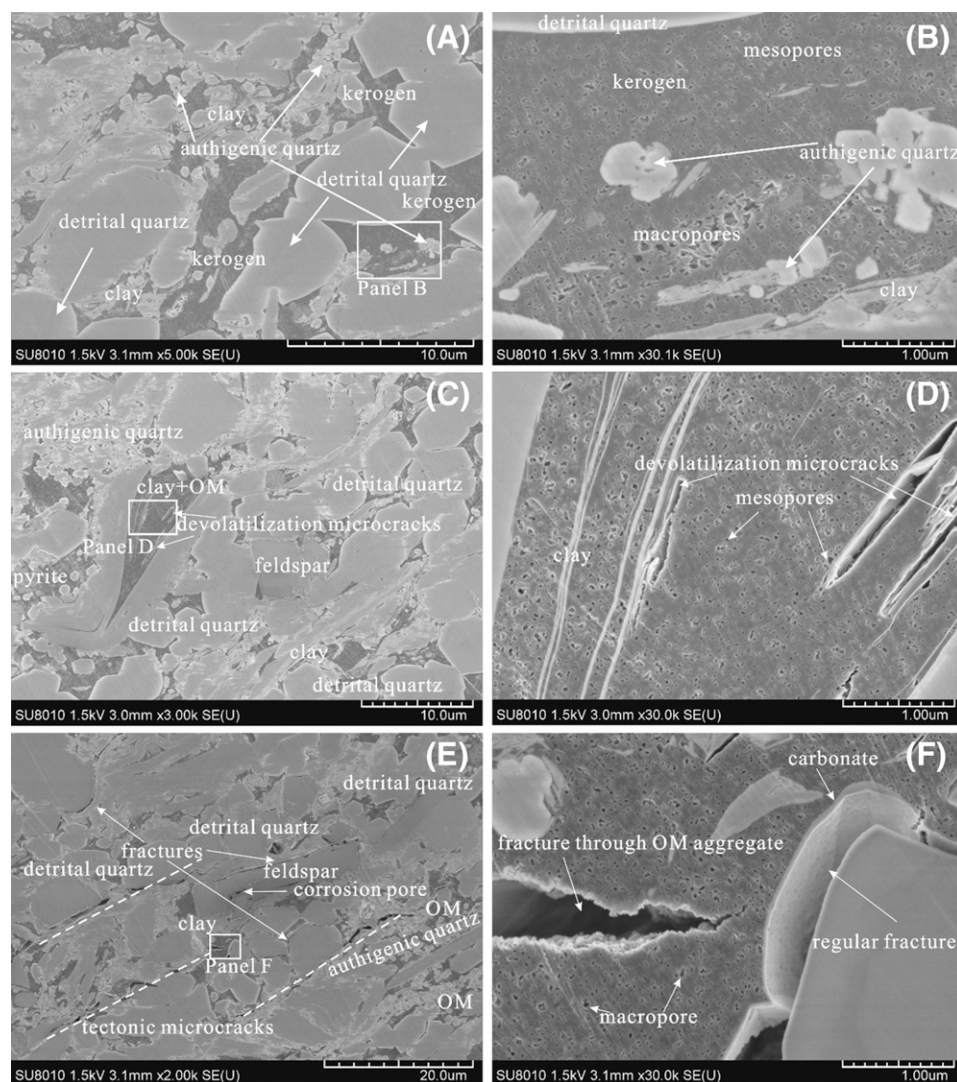
increase in the V_{total} of the shale samples in the detachment layer could be attributed to the increase in mesopores and macropores caused by the development of cracks and microcracks (Liang et al., 2017). However, the micropores can be shielded from compaction and tectonic deformation because of their small pore sizes (Kuila and Prasad, 2013). The increase in mesopores, macropores, and natural microcracks might favor gas release from the shale matrix (Keller et al., 2011; Chalmers et al., 2012a). Additionally, the cracks and microcracks that occur in the detachment layer could increase the connectivity of the shale pore network and provide a lateral migration pathway for shale gas at a regional scale, which could also provide an explanation for why the shale gas fields in the Longmaxi–Wufeng shales share some characteristics with conventional gas fields: for

example, shale gas is enriched in positive structures, especially in anticline traps (Guo and Zeng, 2015).

The Pengye 1 well provides a good example to understand how the detachment layer can influence the preservation conditions of the shale gas of the Wufeng–Longmaxi Formations. The Pengye 1 well is located in the Sangzeping syncline, which is east of the Qiyueshan fault (Guo and Zeng, 2015). The SQ-1 well is also located east of the Qiyueshan fault. Although the Wufeng–Longmaxi shales of the Pengye 1 well are buried deeply (depth 2150 m [7054 ft]) in the syncline (negative tectonics) and only have weak deformation and undeveloped faults, the pressure coefficient is approximately 1.0 (Guo and Zeng, 2015), suggesting that the preservation condition of the Pengye 1 well was at least partially destroyed. This is because the detachment layer could provide an
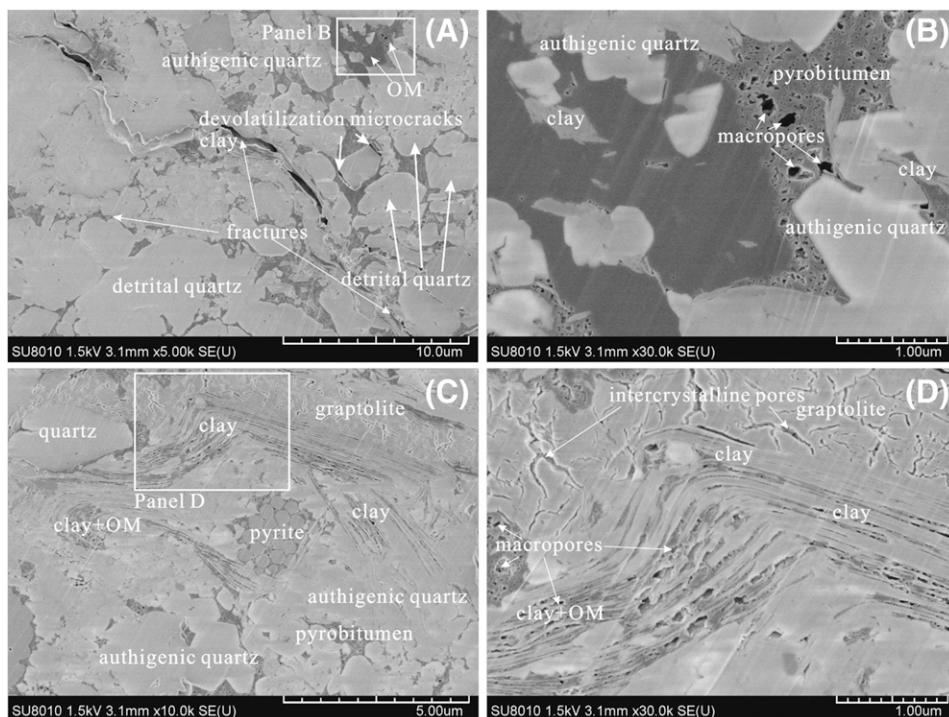
Figure 12. The field emission scanning electron microscopy (FE-SEM) images of the Katian sample, 87.1 m (285.8 ft). (A) A lot of fractures and authigenic quartz among detrital quartz. (B) A patch of organic matter (OM) lacks observable pores. (C) The pore system and minerals in the Katian shale were affected by the tectonic deformation. (D) Coarse mesopores (25–50 nm) and macropores (>50 nm) that were altered by the tectonic deformation.

important pathway for the escape of shale gas in the Wufeng–Longmaxi Formations. In fact, the presence of the detachment layer in the Wufeng Formation makes the preservation conditions a very important factor that controls the shale gas resource potential of the Wufeng–Longmaxi shales on the southeast margin of the Sichuan Basin. The Pengye 1 well also suggests that the preservation condition of shale gas in negative tectonics may be poor because of the existence of the detachment layer. Although the SQ-1 well is located in the saddle of an anticline, the preservation condition of the SQ-1 well is poor because the top of the anticline at Sanquan Town is destroyed and the Wufeng–Longmaxi shale is exposed.

To evaluate the Wufeng–Longmaxi shales in Sanquan Town, the characteristics of the shales from the SQ-1 well were compared with those of the Jiaoye 1 (JY1) well in the Jiaoshiba shale gas field. The Jiaoshiba shale gas field is a highly productive shale gas field in the Sichuan Basin. The thickness of the high-quality shale intervals (TOC > 2.0 wt. %) is 38 m (125 ft) for the JY1 well, the average TOC value is 3.5 wt. %, and the porosity is 5.1% for the high-quality shale intervals (Guo and Zhang, 2014; Guo et al., 2014a). However, the thickness of the high-quality shale intervals is approximately 24 m (~79 ft)

for the SQ-1 well, the average TOC content is 3.0 wt. %, and the porosity is 4.1% for the high-quality shale intervals. In other words, the thickness, TOC contents, and porosity of the high-quality shale intervals in the SQ-1 well are significantly lower than those of the JY1 well. Therefore, the Wufeng–Longmaxi marine shales of the JY1 well have better preservation conditions and resource potential than those of the SQ-1 well (Figure 16).

Figure 13. Scratches on the surface of the detachment layer in the Katian, 87.8 m (288.1 ft).
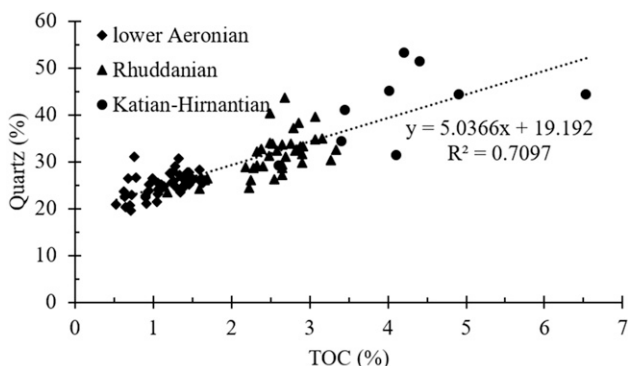
Figure 14. The relationship between the total organic carbon (TOC) content and quartz content. A positive linear relationship indicates that a part of the quartz in the Rhuddanian, Hirnantian, and Katian shales may have a biogenic origin. R^2 = coefficient of determination.

In addition, there are many similarities in the geochemical parameters between the SQ-1 well and JY1 well. For example, the R_{equ} values of the SQ-1 well and JY1 well were in the ranges of 2.14%–2.76% (Table 1) and 2.20%–3.06% (Guo and Zhang, 2014), respectively, indicating that the Wufeng–Longmaxi shales of both wells are at an overmature stage. The organic transformation ratio (TR) is the conversion rate of the original OM into liquid and gaseous hydrocarbons during maturation (Jarvie et. al., 2007). If the current hydrocarbon potential was zero, TR could be thought to reach 100%. However, no low-maturity Wufeng–Longmaxi shale samples are available to evaluate the original hydrocarbon and gas potentials. Since the high-quality shale intervals of both wells are at an overmature stage and the residual hydrocarbon potentials are very close to zero (Table 1), the TR values of shale samples from both wells are at 99%. Furthermore, the average brittle mineral content of the high-quality shale intervals in the SQ-1 well is 59.1%, slightly lower than that of the JY1 well (62.4%). Therefore, although the shale samples in the SQ-1 well are slightly lower in the thickness, TOC contents, and porosity of the high-quality shale intervals than those of the JY1 well to some extent, they have similar maturity, organic TR ratios, and mineral compositions. Considering that the type of kerogen, thermal maturity, and other geochemical parameters are similar to those in the Jiaoshiba shale gas field, the Wufeng–Longmaxi shales in Sanquan Town must have a considerably good shale gas generation potential, which refers to the conversion potential of

both kerogen and retained oil into gas from low maturity to high maturity (Jarvie et al., 2007).

However, there are significant differences between Jiaoshiba Town and Sanquan Town in regard to their preservation and tectonic conditions. The JY1 well is located in the Jiaoshiba structure, which is located west of the Qiyueshan fault. The main body of the Jiaoshiba structure is a box-like, gently faulted anticline with weak deformation and undeveloped faults. The burial depth of the Longmaxi Formation is approximately 2300 m (~7546 ft), and its pressure coefficient is approximately 1.55 (Guo and Zhang, 2014). However, Sanquan Town includes the Jinfoshan syncline and two anticlines (the Longguxi anticline and Jianzishan anticline), and the SQ-1 well is located at the saddle of the anticline, which contains outcrops that are rich in faults that formed during a time of earlier uplift (Figure 1B). These observations indicate that the preservation and tectonic conditions in Sanquan were not as good as those in Jiaoshiba.
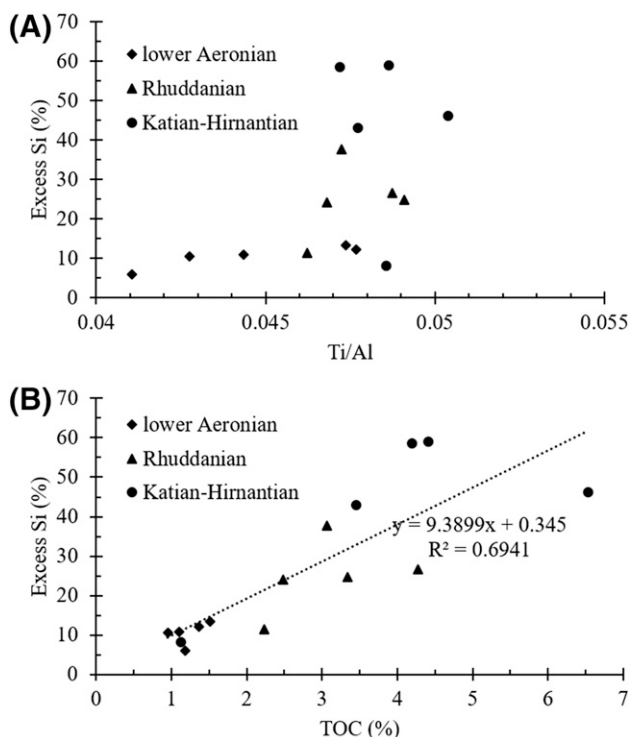

Figure 15. (A) The relationship between the excess silica (Si_{excess}) and TiO_2/Al_2O_3 (Ti/Al), suggesting that shale samples with high excess silica content were mainly developed at high Ti/Al stage. (B) The relationship between the Si_{excess} and total organic carbon (TOC) content. A good positive relationship exists between the excess silica content and TOC content, and the trend line almost passes through the origin. R^2 = coefficient of determination.

Therefore, the shale gas prospect of Sanquan should be very limited although the shales in this area have considerable shale gas generation potential.

CONCLUSIONS

To study the marine Wufeng–Longmaxi shale in Sanquan along the southeast margin of the Sichuan Basin, an approximately 100-m-deep (~328-ft-deep) well was drilled in Sanquan Town of the Nanchuan District, Chongqing Municipality. The geochemical data indicated a high-quality shale interval (TOC > 2.0 wt. %, clay < 40%) that is approximately 24 m (~79 ft) thick, with an average TOC value of 3.0 wt. %. High-quality shales with a high TOC and high brittle mineral content were mainly deposited in the Katian, Hirnantian, and Rhuddanian. The lithology of the high-quality shale interval mainly includes siliceous shale and carbonaceous shale in the TST and HST. The variations in the porosity, specific surface area, and

nanopore structure distribution were mainly related to the variations in the TOC of shales. Higher TOC values commonly lead to a higher porosity and specific surface area. Basically, the TOC values and content of brittle minerals, especially the silica content, decrease upward from the Katian to the Rhuddanian and Aeronian.

Tectonic movements may also be a very important factor that influences the petrophysical properties of the Wufeng–Longmaxi shales as well as the preservation potential of the shale gas. The coarse mesopore volume and macropore volume of the shale samples in the Katian were significantly augmented in the detachment layer because of the cracks and microcracks that were produced by complex tectonic movements. Additionally, the microcracks in the detachment layer can connect more pores and improve the connectivity of the shale. Furthermore, the detachment layer may also provide a lateral migration pathway for shale gas at a regional scale. The extensive occurrence of the detachment layer makes the preservation condition an
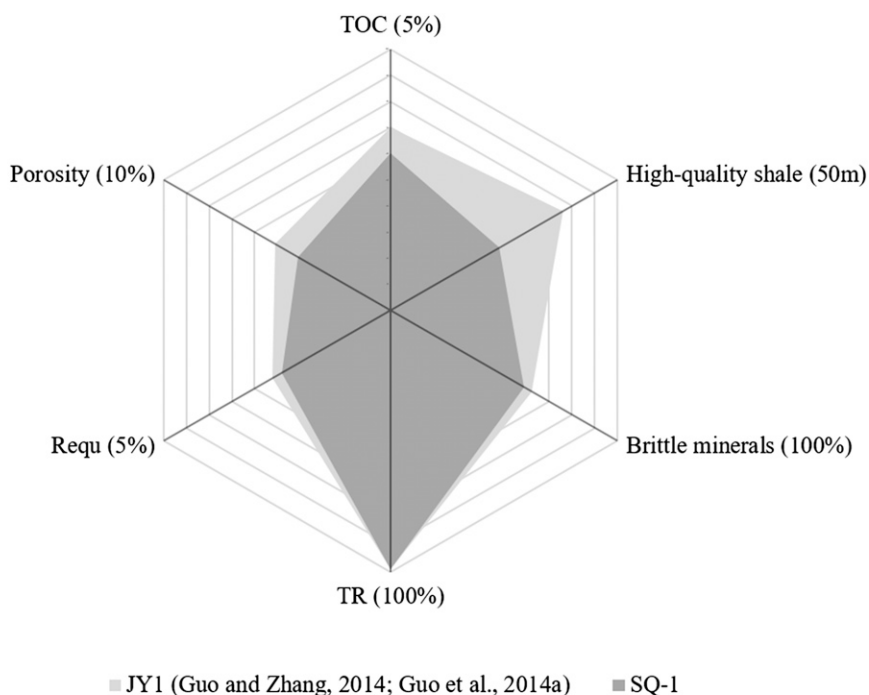

Figure 16. The comparison of characteristics of the Wufeng–Longmaxi shales from the Sanquan-1 (SQ-1) and Jiaoye 1 (JY1) wells. Brittle minerals are quartz, feldspar, carbonates, and pyrite; high-quality shale is shale with total organic carbon (TOC) content greater than 2.0 wt. %. R_{equ} = equivalent vitrinite reflectance; TR = the transformation rate of the original organic matter into liquid and gaseous hydrocarbons during maturation.

■ JY1 (Guo and Zhang, 2014; Guo et al., 2014a)   ■ SQ-1

	JY1	SQ-1
TOC (%)	3.5	3.0
High-quality shale (m)	38.0	24.0
Brittle minerals (%)	62.4	59.1
Porosity (%)	5.1	4.1
TR (%)	99.0	99.0
Requ (%)	2.20-3.06 (2.6)	2.14-2.76 (2.4)

important factor that can influence the final shale gas prospect. Compared with the Wufeng–Longmaxi shales from the JY1 well of the Jiaoshiba shale gas field, those from the SQ-1 well in Sanquan Town have a considerably good shale gas generation potential. However, the shale gas prospect of Sanquan may be very limited because the detachment layer that resulted from complex tectonic movements may accelerate the escape of shale gas from the shale matrix in destroyed anticlines in this area.

REFERENCES CITED

Arthur, M. A., and B. B. Sageman, 1994, Marine black shales: Depositional mechanisms and environments of ancient deposits: Annual Review of Earth and Planetary Sciences, v. 22, no. 1, p. 499–551, doi:10.1146/annurev.ea.22.050194.002435.

Behar, F., V. Beaumont, and H. L. De B. Penteado, 2001, Rock-Eval 6 technology: Performances and developments: Oil & Gas Science and Technology, v. 56, no. 2, p. 111–134, doi:10.2516/ogst:2001013.

Bernard, S., R. Wirth, A. Schreiber, H. Schulz, and B. Horsfield, 2012, Formation of nanoporous pyrobitumen residues during maturation processes within the Barnett Shale (Fort Worth Basin): International Journal of Coal Geology, v. 103, no. 23, p. 3–11, doi:10.1016/j.coal.2012.04.010.

Bolton, A. J., A. J. Maltmn, and Q. Fisher, 2000, Anisotropic permeability and bimodal pore-size distributions of fine-grained marine sediments: Marine and Petroleum Geology, v. 17, no. 6, p. 657–672, doi:10.1016/S0264-8172(00)00019-2.

Brenchley, P., G. Carden, L. Hints, D. Kaljo, J. Marshall, T. Martma, T. Meidla, and J. Nõlvak, 2003, High-resolution stable isotope stratigraphy of Upper Ordovician sequences: Constraints on the timing of bioevents and environmental changes associated with mass extinction and glaciation: Geological Society of America Bulletin, v. 115, no. 1, p. 89–104, doi:10.1130/0016-7606(2003)115<0089:HRSISO>2.0.CO;2.

Cao, H. Y., C. Q. Zhu, and N. S. Qin, 2015b, Thermal evolution of Lower Silurian Longmaxi Formation in the eastern Sichuan Basin (in Chinese): Journal of Earth Sciences and Environment, v. 37, no. 6, p. 22–32.

Cao, T. T., Z. G. Song, S. B. Wang, X. X. Cao, Y. Li, and J. Xia, 2015a, Characterizing the pore structure in the Silurian and Permian shales of the Sichuan Basin, China: Marine and Petroleum Geology, v. 61, no. 3, p. 140–150, doi:10.1016/j.marpetgeo.2014.12.007.

Caplan, M. L., and R. M. Bustin, 1998, Sedimentology and sequence stratigraphy of Devonian-Carboniferous strata, southern Alberta: Bulletin of Canadian Petroleum Geology, v. 46, no. 4, p. 487–514.

Chalmers, G. R. L., R. M. Bustin, and I. M. Power, 2012a, Characterization of gas shale pore systems by porosimetry, pycnometry, surface area, and field emission scanning electron microscopy/transmission electron microscopy image analyses: Examples from the Barnett, Woodford, Haynesville, Marcellus, and Doig units: AAPG Bulletin, v. 96, no. 6, p. 1099–1119, doi:10.1306/10171111052.

Chalmers, G. R. L., D. J. K. Ross, and R. M. Bustin, 2012b, Geological controls on matrix permeability of Devonian Gas Shales in the Horn River and Liard basins, northeastern British Columbia, Canada: International Journal of Coal Geology, v. 103, p. 120–131, doi:10.1016/j.coal.2012.05.006.

Chen, L., Y. C. Lu, S. Jiang, J. Q. Li, T. L. Guo, and C. Luo, 2015, Heterogeneity of the Lower Silurian Longmaxi marine shale in the southeast Sichuan Basin of China: Marine and Petroleum Geology, v. 65, p. 232–246, doi:10.1016/j.marpetgeo.2015.04.003.

Chen, X., J. X. Fan, Q. Chen, L. Tang, and X. D. Hou, 2014, Toward a stepwise Kwangsian Orogeny: Science China. Earth Sciences, v. 57, no. 3, p. 379–387, doi:10.1007/s11430-013-4815-y.

Chen, X., J. Y. Rong, J. X. Fan, R. B. Zhan, C. E. Mitchell, D. A. T. Harper, M. J. Melchin, P. A. Peng, S. C. Finney, and X. F. Wang, 2006, A final report on the global stratotype section and point (GSSP) for the Hirnantian stage (Upper Ordovician) (in Chinese): Journal of Stratigraphy, v. 30, no. 4, p. 289–305.

Clarkson, C. R., M. Freeman, L. He, M. Agamalian, Y. B. Melnichenko, M. Mastalerz, R. M. Bustin, A. P. Radlinski, and T. P. Blach, 2012, Characterization of tight gas reservoir pore structure using USANS/SANS and gas adsorption analysis: Fuel, v. 95, no. 1, p. 371–385, doi:10.1016/j.fuel.2011.12.010.

Curtis, J. B., 2002, Fractured shale-gas systems: AAPG Bulletin, v. 86, no. 11, p. 1921–1938, doi:10.1306/61eeddbe-173e-11d7-8645000102c1865d.

Curtis, M. E., B. J. Cardott, C. H. Sondergeld, and C. S. Rai, 2012, Development of organic porosity in the Woodford Shale with increasing thermal maturity: International Journal of Coal Geology, v. 103, p. 26–31, doi:10.1016/j.coal.2012.08.004.

Fan, J. X., J. M. Melchin, X. Chen, Y. Wang, Y. D. Zhang, Q. Chen, Z. L. Chi, and F. Chen, 2011, Biostratigraphy and geography of the Ordovician-Silurian Lungmachi black shales in South China: Science China. Earth Sciences, v. 54, no. 12, p. 1854–1863, doi:10.1007/s11430-011-4301-3.

Finnegan, S., K. Bergmann, J. M. Eiler, D. S. Jones, D. A. Fike, I. Eisenman, N. C. Hughes, A. K. Tripati, and W. W. Fischer, 2011, The magnitude and duration of Late Ordovician–Early Silurian glaciation: Science, v. 331, no. 6019, p. 903–906, doi:10.1126/science.1200803.

Guo, T. L., and R. B. Liu, 2013, Implications from marine shale gas exploration breakthrough in complicated structural area at high thermal stage: Taking Longmaxi Formation in well JY1 as an example: Natural Gas Geoscience, v. 24, no. 4, p. 643–651.

Guo, T. L., and P. Zeng, 2015, The structural and preservation conditions for shale gas enrichment and high productivity in the Wufeng-Longmaxi Formation: Southeastern Sichuan Basin: Energy Exploration and Exploitation, v. 33, no. 3, p. 259–276, doi:10.1260/0144-5987.33.3.259.

Guo, T. L., and H. R. Zhang, 2014, Formation and enrichment mode of Jiaoshiba shale gas field, Sichuan Basin: Petroleum Exploration and Development, v. 41, no. 1, p. 31–40, doi:10.1016/S1876-3804(14)60003-3.

Guo, X. S., 2014, Enrichment mechanism and exploration technology of Fuling shale gas field at Jiaoshiba Block (in Chinese): Beijing, China, Science Press, p. 3–5.

Guo, X. S., D. F. Hu, Y. P. Li, X. F. Wei, Q. B. Wang, and H. Zhang, 2016, Technologies in discovery and exploration of Fuling Shale Gas Field, China: Natural Resources, v. 7, no. 5, p. 271–286, doi:10.4236/nr.2016.75024.

Guo, X. S., D. F. Hu, Z. D. Wen, and R. B. Liu, 2014a, Major factors controlling the accumulation and high productivity in marine shale gas in the Lower Paleozoic of Sichuan Basin and its periphery: A case study of the Wufeng-Longmaxi Formation of Jiaoshiba area: Geology in China, v. 41, no. 3, p. 893–901.

Guo, X. S., Y. P. Li, R. B. Liu, and Q. B. Wang, 2014b, Characteristics and controlling factors of micropore structures of the Longmaxi Shale in the Jiaoshiba area, Sichuan Basin: Natural Gas Industry B, v. 1, no. 2, p. 165–171, doi:10.1016/j.ngib.2014.11.007.

Hao, F., H. Y. Zou, and Y. C. Lu, 2013, Mechanisms of shale gas storage: Implications for shale gas exploration in China: AAPG Bulletin, v. 97, no. 8, p. 1325–1346, doi:10.1306/02141312091.

Hunt, J. M., 1996, Petroleum geochemistry and geology, 2nd ed.: New York, W. H. Freeman, 743 p.

International Union of Pure and Applied Chemistry, 1994, Recommendations for the characterization of porous solids (technical report): Pure and Applied Chemistry, v. 66, no. 8, p. 1739–1758, doi:10.1351/pac199466081739.

Jarvie, D. M., R. J. Hill, T. E. Ruble, and R. M. Pollastro, 2007, Unconventional shale-gas systems: The Mississippian Barnett Shale of north-central Texas as one model for thermogenic shale-gas assessment: AAPG Bulletin, v. 91, no. 4, p. 475–499, doi:10.1306/12190606068.

Ji, W. M., Y. Song, Z. X. Jiang, L. Chen, Z. Li, X. Yang, and M. M. Meng, 2015, Estimation of marine shale methane adsorption capacity based on experimental investigations of Lower Silurian Longmaxi formation in the Upper Yangtze Platform, south China: Marine and Petroleum Geology, v. 68, p. 94–106, doi:10.1016/j.marpetgeo.2015.08.012.

Jin, L., R. Mathur, G. Rother, D. Cole, E. Bazilevskaya, J. Williams, A. Carone, and S. Brantley, 2013, Evolution of porosity and geochemistry in Marcellus Formation black shale during weathering: Chemical Geology, v. 356, p. 50–63, doi:10.1016/j.chemgeo.2013.07.012.

Keller, L. M., L. Holzer, R. Wepf, and P. Gasser, 2011, 3D geometry and topology of pore pathways in Opalinus clay: Implications for mass transport: Applied Clay Science, v. 52, no. 1–2, p. 85–95, doi:10.1016/j.clay.2011.02.003.

Kuila, U., and M. Prasad, 2013, Specific surface area and pore-size distribution in clays and shales: Geophysical Prospecting, v. 61, no. 2, p. 341–362, doi:10.1111/1365-2478.12028.

Li, X. J., S. Y. Hu, and K. M. Cheng, 2007, Suggestions from the development of fractured shale gas in North America: Petroleum Exploration and Development, v. 34, no. 4, p. 392–400.

Li, Y. F., T. W. Zhang, G. S. Ellis, and D. Y. Shao, 2017, Depositional environment and organic matter accumulation of Upper Ordovician–Lower Silurian marine shale in the Upper Yangtze Platform, South China: Palaeogeography, Palaeoclimatology, Palaeoecology, v. 466, p. 252–264, doi:10.1016/j.palaeo.2016.11.037.

Liang, C., Z. X. Jiang, Y. C. Cao, M. H. Wu, L. Guo, and C. M. Zhang, 2016, Deep-water depositional mechanisms and significance for unconventional hydrocarbon exploration: A case study from the lower Silurian Longmaxi shale in the southeastern Sichuan Basin: AAPG Bulletin, v. 100, no. 5, p. 773–794, doi:10.1306/02031615002.

Liang, C., Z. X. Jiang, Y. T. Yang, and X. J. Wei, 2012, Shale lithofacies and reservoir space of the Wufeng-Longmaxi Formation, Sichuan Basin, China: Petroleum Exploration and Development, v. 39, no. 6, p. 736–743, doi:10.1016/S1876-3804(12)60098-6.

Liang, C., Z. X. Jiang, C. M. Zhang, L. Guo, Y. T. Yang, and J. Li, 2014, The shale characteristics and shale gas exploration prospects of the Lower Silurian Longmaxi shale, Sichuan Basin, South China: Journal of Natural Gas Science and Engineering, v. 21, p. 636–648, doi:10.1016/j.jngse.2014.09.034.

Liang, M. L., Z. X. Wang, L. Gao, C. L. Li, and H. J. Li, 2017, Evolution of pore structure in gas shale related to structural deformation: Fuel, v. 197, p. 310–319, doi:10.1016/j.fuel.2017.02.035.

Liu, Y., C. Li, T. J. Algeo, J. X. Fan, and P. A. Peng, 2016, Global and regional controls on marine redox changes across the Ordovician-Silurian boundary in South China: Palaeogeography, Palaeoclimatology, Palaeoecology, v. 463, p. 180–191, doi:10.1016/j.palaeo.2016.10.006.

Loucks, R. G., and R. M. Reed, 2014, Scanning-electron-microscope petrographic evidence for distinguishing organic-matter pores associated with depositional organic matter versus migrated organic matter in mudrocks: Gulf Coast Association of Geological Societies Journal, v. 3, p. 51–60.

Loucks, R. G., R. M. Reed, S. C. Ruppel, and U. Hammes, 2012, Spectrum of pore types and networks in mudrocks and a descriptive classification for matrix-related mudrock pores: AAPG Bulletin, v. 96, no. 6, p. 1071–1098, doi:10.1306/08171111061.

Loucks, R. G., R. M. Reed, S. C. Ruppel, and D. M. Jarvie, 2009, Morphology, genesis, and distribution of nanometer-scale pores in siliceous mudstones of the Mississippian Barnett Shale: Journal of Sedimentary Research, v. 79, no. 12, p. 848–861, doi:10.2110/jsr.2009.092.

Luo, Q. Y., N. N. Zhong, N. Dai, and W. Zhang, 2016, Graptolite-derived organic matter in the Wufeng–Longmaxi Formations (Upper Ordovician–Lower Silurian) of southeastern Chongqing, China: Implications for gas shale evaluation: International Journal of Coal Geology, v. 153, no. 1–2, p. 87–98, doi:10.1016/j.coal.2015.11.014.

Ma, Y., N. N. Zhong, L. J. Cheng, Z. J. Pan, N. Dai, Y. Zhang, and L. Yang, 2016, Pore structure of the graptolite-derived OM in the Longmaxi Shale, southeastern Upper Yangtze Region, China: Marine and Petroleum Geology, v. 72, p. 1–11, doi:10.1016/j.marpetgeo.2016.01.009.

Mastalerz, M., A. Schimmelmann, A. Drobniak, and Y. Chen, 2013, Porosity of Devonian and Mississippian New Albany Shale across a maturation gradient: Insights from organic petrology, gas adsorption, and mercury intrusion: AAPG Bulletin, v. 97, no. 10, p. 1621–1643, doi:10.1306/04011312194.

Milliken, K. L., M. Rudnicki, D. N. Awwiller, and T. Zhang, 2013, Organic matter hosted pore system, Marcellus formation (Devonian), Pennsylvania: AAPG Bulletin, v. 97, no. 2, p. 177–200, doi:10.1306/07231212048.

Murphy, A. E., B. B. Sageman, D. J. Hollander, T. W. Lyons, and C. E. Brett, 2000, Black shale deposition and faunal overturn in the Devonian Appalachian Basin: Clastic starvation, seasonal water–column mixing, and efficient biolimiting nutrient recycling: Paleoceanography, v. 15, no. 3, p. 280–291, doi:10.1029/1999PA000445.

Nie, H. K., S. J. Bao, B. Gao, R. K. Bian, and J. C. Zhang, 2012, Accumulation system for shale gas from Upper Ordovician to Lower Silurian in Sichuan Basin and surrounding areas (in Chinese): Petroleum Geology and Experiment, v. 34, no. 2, p. 115–119.

Peltonen, C., Ø. Marcussen, K. Bjørlykke, and J. Jahren, 2009, Clay mineral diagenesis and quartz cementation in mudstones: The effects of smectite to illite reaction on rock properties: Marine and Petroleum Geology, v. 26, no. 6, p. 887–898, doi:10.1016/j.marpetgeo.2008.01.021.

Ravikovitch, P. I., and A. V. Neimark, 2006, Density functional theory model of adsorption on amorphous and microporous silica materials: Langmuir, v. 22, no. 26, p. 11171–11179, doi:10.1021/la0616146.

Rimmer, S. M., J. A. Thompson, S. A. Goodnight, and T. L. Robl, 2004, Multiple controls on the preservation of organic matter in Devonian–Mississippian marine black shales: Geochemical and petrographic evidence: Palaeogeography, Palaeoclimatology, Palaeoecology, v. 215, no. 1–2, p. 125–154, doi:10.1016/S0031-0182(04)00466-3.

Ross, D. J. K., and R. M. Bustin, 2008, Characterizing the shale gas resource potential of Devonian-Mississippian strata in the Western Canada sedimentary basin: Application of an integrated formation evaluation: AAPG Bulletin, v. 92, no. 1, p. 87–125, doi:10.1306/09040707048.

Ross, D. J. K., and R. M. Bustin, 2009a, Investigating the use of sedimentary geochemical proxies for paleoenvironment interpretation of thermally mature organic-rich strata: Examples from the Devonian-Mississippian shales, Western Canadian Sedimentary Basin: Chemical Geology, v. 260, no. 1–2, p. 1–19, doi:10.1016/j.chemgeo.2008.10.027.

Ross, D. J. K., and R. M. Bustin, 2009b, The importance of shale composition and pore structure upon gas storage potential of shale gas reservoirs: Marine and Petroleum Geology, v. 26, no. 6, p. 916–927, doi:10.1016/j.marpetgeo.2008.06.004.

Rouquerol, J., and F. Rouquerol, 2014, Adsorption at the liquid–solid interface: Thermodynamics and methodology, in J. Rouquerol, F. Rouquerol, K. S. W. Sing, P. Llewellyn, and G. Maurin, eds., Adsorption by powders and porous solids: Principles, methodology and applications, 2nd ed.: New York, Academic Press, p. 105–158, doi:10.1016/B978-0-08-097035-6.00004-8.

Rowley, D. B., 1996, Age of initiation of collision between India and Asia: A review of stratigraphic data: Earth and Planetary Science Letters, v. 145, no. 1–4, p. 1–13, doi:10.1016/S0012-821X(96)00201-4.

Schieber, J., D. Krinsley, and L. Riciputi, 2000, Diagenetic origin of quartz silt in mudstones and implications for silica cycling: Nature, v. 406, no. 6799, p. 981–985, doi:10.1038/35023143.

Schoenherr, J., R. Littke, J. L. Urai, P. A. Kukla, and Z. Rawahi, 2007, Polyphase thermal evolution in the Infra-Cambrian Ara Group (South Oman Salt Basin) as deduced by maturity of solid reservoir bitumen: Organic Geochemistry, v. 38, no. 8, p. 1293–1318, doi:10.1016/j.orggeochem.2007.03.010.

Shen, C. B., L. F. Mei, Z. P. Xu, and J. G. Tang, 2007, Architecture and tectonic evolution of composite basin-mountain system in Sichuan Basin and its adjacent areas (in Chinese): Geotectonica et Metallogenia, v. 31, no. 3, p. 288–299.

Slatt, R. M., and N. D. Rodriguez, 2012, Comparative sequence stratigraphy and organic geochemistry of gas shales: Commonality or coincidence?: Journal of Natural Gas Science and Engineering, v. 8, p. 68–84, doi:10.1016/j.jngse.2012.01.008.

Strapoć, D., M. Mastalerz, A. Schimmelmann, A. Drobniak, and N. R. Hasenmueller, 2010, Geochemical constraints on the origin and volume of gas in the New Albany Shale (Devonian–Mississippian), eastern Illinois Basin: AAPG Bulletin, v. 94, no. 11, p. 1713–1740, doi:10.1306/06301009197.

Tang, X. L., Z. X. Jiang, Z. Li, Z. Y. Gao, Y. Q. Bai, S. Zhao, and J. Feng, 2015, The effect of the variation in material composition on the heterogeneous pore structure of high-maturity shale of the Silurian Longmaxi formation in the southeastern Sichuan Basin, China: Journal of Natural Gas Science and Engineering, v. 23, p. 464–473, doi:10.1016/j.jngse.2015.02.031.

Thommes, M., and K. A. Cychosz, 2014, Physical adsorption characterization of nanoporous materials: Progress and challenges: Adsorption, v. 20, no. 2–3, p. 233–250, doi:10.1007/s10450-014-9606-z.

Tian, H., L. Pan, X. M. Xiao, R. W. T. Wilkins, Z. P. Meng, and B. J. Huang, 2013, A preliminary study on the pore characterization of Lower Silurian black shales in the Chuandong Thrust Fold Belt, southwestern China using low pressure N_2 adsorption and FE-SEM methods: Marine and Petroleum Geology, v. 48, p. 8–19, doi:10.1016/j.marpetgeo.2013.07.008.

Wang, S. B., Z. G. Song, T. T. Cao, and X. Song, 2013, The methane sorption capacity of Paleozoic shales from the Sichuan Basin, China: Marine and Petroleum Geology, v. 44, p. 112–119, doi:10.1016/j.marpetgeo.2013.03.007.

Wang, S. F., C. N. Zhou, D. Z. Dong, Y. M. Wang, J. L. Huang, and Z. J. Hou, 2014, Biogenic silica of organic-rich shale in Sichuan Basin and its significance for shale gas (in Chinese): Beijing Da Xue Xue Bao. Zi Ran Ke Xue Bao, v. 50, no. 3, p. 476–486.

Wang, T., K. M. Yang, L. Xiong, H. L. Shi, Q. L. Zhang, L. M. Wei, and X. L. He, 2015a, Shale sequence stratigraphy of Wufeng-Longmaxi Formation in southern Sichuan and their control on reservoirs (in Chinese): Acta Petrolei Sinica, v. 36, no. 8, p. 915–925.

Wang, Y. M., D. Z. Dong, X. J. Li, J. L. Huang, S. F. Wang, and W. Wu, 2015b, Stratigraphic sequence and sedimentary characteristics of Lower Silurian Longmaxi Formation in Sichuan Basin and its peripheral areas: Natural Gas Industry B, v. 2, no. 2–3, p. 222–232, doi:10.1016/j.ngib.2015.07.014.

Wang, Y. M., J. L. Huang, X. J. Li, D. Z. Dong, S. F. Wang, and Q. Z. Guan, 2015c, Quantitative characterization of fractures and pores in shale beds of the Lower Silurian, Longmaxi Formation, Sichuan Basin: Natural Gas Industry B, v. 2, no. 6, p. 481–488, doi:10.1016/j.ngib.2015.12.002.

Wedepohl, K. H., 1971, Environmental influences on the chemical composition of shales and clays: Physics and Chemistry of the Earth, v. 8, no. 71, p. 305–333, doi:10.1016/0079-1946(71)90020-6.

Wedepohl, K. H., 1991, The composition of the upper earth's crust and the natural cycles of selected metals. Metals in natural raw materials: Natural resources, in E. Merian, ed., Metals and their compounds in the environment: Weinheim, Germany, VCH, p. 3–17.

Wei, M. M., L. Zhang, Y. Q. Xiong, J. H. Li, and P. A. Peng, 2016, Nanopore structure characterization for organic-rich shale using the non-local-density functional theory by a combination of N_2 and CO_2 adsorption: Microporous and mesoporous materials, v. 227, p. 88–94, doi:10.1016/j.micromeso.2016.02.050.

Xu, W., M. Ruhl, H. C. Jenkyns, S. P. Hesselbo, J. B. Riding, D. Selby, B. D. A. Naafs, J. W. H. Weijers, R. D. Pancost, and E. W. Tegelaar, 2017, Carbon sequestration in an expanded lake system during the Toarcian oceanic anoxic event: Nature Geoscience, v. 10, no. 2, p. 129–134, doi:10.1038/ngeo2871.

Yan, D. P., M. F. Zhou, H. L. Song, X. W. Wang, and J. Malpas, 2003, Origin and tectonic significance of a Mesozoic multilayer over-thrust system within the Yangtze Block (South China): Tectonophysics, v. 361, no. 3–4, p. 239–254, doi:10.1016/S0040-1951(02)00646-7.

Yang, R., S. He, J. Z. Yi, and Q. H. Hu, 2016, Nano-scale pore structure and fractal dimension of organic-rich Wufeng-Longmaxi shale from Jiaoshiba area, Sichuan Basin: Investigations using FE-SEM, gas adsorption and helium pycnometry: Marine and Petroleum Geology, v. 70, p. 27–45, doi:10.1016/j.marpetgeo.2015.11.019.

Yuan, Y. S., J. H. Lin, X. Y. Cheng, and S. J. Li, 2014, Yanshan-Himalayan denudation in Western Hubei Eastern Chongqing area (in Chinese): Chinese Journal of Geophysics, v. 57, no. 6, p. 809–817, doi:10.1002/cjg2.20144.

Zeng, X. L., S. G. Liu, and C. J. Zhang, 2011, Comparison of Silurian Longmaxi Formation shale of Sichuan Basin in China and Carboniferous Barnett Formation shale of Fort Worth Basin in United States (in Chinese): Geological Bulletin of China, v. 30, no. 2–3, p. 372–384.

Zhang, Z. L., and Z. H. Yang, 2013, Theoretical and practical discussion of measurement accuracy for physisorption with micro- and mesoporous materials: Chinese Journal of Catalysis, v. 34, no. 10, p. 1797–1810, doi:10.1016/S1872-2067(12)60601-9.

Zhao, J. H., Z. K. Jin, Z. J. Jin, X. Wen, and Y. K. Geng, 2017, Origin of authigenic quartz in organic-rich shales of the Wufeng and Longmaxi Formations in the Sichuan Basin, South China: Implications for pore evolution: Journal of Natural Gas Science and Engineering, v. 38, p. 21–38, doi:10.1016/j.jngse.2016.11.037.

Zheng, H. R., B. Gao, Y. Peng, H. Nie, and F. Yang, 2013, Sedimentary evolution and shale gas exploration direction of the Lower Silurian in Middle-Upper Yangtze area (in Chinese): Journal of Palaeogeography, v. 15, no. 5, p. 645–656.

Zou, C. N., Z. Yang, J. X. Dai, D. Z. Dong, B. M. Zhang, Y. M. Wang, S. H. Deng et al., 2015, The characteristics and significance of conventional and unconventional Sinian–Silurian gas systems in the Sichuan Basin, central China: Marine and Petroleum Geology, v. 64, p. 386–402, doi:10.1016/j.marpetgeo.2015.03.005.